Journal Pre-proofs

Red blood cell membrane-camouflaged gold-core silica shell nanorods for cancer drug delivery and photothermal therapy

Carolina F. Rodrigues, Ilídio J. Correia, André F. Moreira

PII: S0378-5173(24)00241-2
DOI: https://doi.org/10.1016/j.ijpharm.2024.124007
Reference: IJP 124007

To appear in: *International Journal of Pharmaceutics*

Received Date: 27 November 2023
Revised Date: 27 February 2024
Accepted Date: 14 March 2024

Please cite this article as: C.F. Rodrigues, I.J. Correia, A.F. Moreira, Red blood cell membrane-camouflaged gold-core silica shell nanorods for cancer drug delivery and photothermal therapy, *International Journal of Pharmaceutics* (2024), doi: https://doi.org/10.1016/j.ijpharm.2024.124007

Red blood cell membrane-camouflaged gold-core silica shell nanorods for cancer drug delivery and photothermal therapy

Carolina F. Rodrigues[1], Ilídio J. Correia[1,2,3*], André F. Moreira[1,4*]

[1]CICS-UBI – Health Sciences Research Centre, University of Beira Interior, Av. Infante D. Henrique, 6200-506 Covilhã, Portugal.

[2]CIEPQPF – Departamento de Engenharia Química, Universidade de Coimbra, Rua Sílvio Lima, 3030-790 Coimbra, Portugal.

[3]AEROG-LAETA, Aerospace Sciences Department, Universidade da Beira Interior, Covilhã, Portugal.

[4]CPIRN-UDI/IPG - Centro de Potencial e Inovação em Recursos Naturais, Unidade de Investigação para o Desenvolvimento do Interior do Instituto Politécnico da Guarda, Avenida Dr. Francisco de Sá Carneiro, No. 50, 6300-559 Guarda, Portugal.

*Corresponding authors. Tel.: +351 275 329 002; e-mail: icorreia@ubi.pt and afmoreira@fcsaude.ubi.pt.

Abstract

Gold core mesoporous silica shell (AuMSS) nanorods are multifunctional nanomedicines that can act simultaneously as photothermal, drug delivery, and bioimaging agents. Nevertheless, it is reported that once administrated, nanoparticles can be coated with blood proteins, forming a protein corona, that directly impacts on nanomedicines' circulation time, biodistribution, and therapeutic performance. Therefore, it become crucial to develop novel alternatives to improve nanoparticles' half-life in the bloodstream. In this work, Polyethylenimine (PEI) and Red blood cells (RBC)-derived membranes were combined for the first time to functionalize AuMSS nanorods and simultaneously load acridine orange (AO). The obtained results revealed that the RBC-derived membranes promoted the neutralization of the AuMSS' surface charge and consequently improved the colloidal stability and biocompatibility of the nanocarriers. Indeed, the *in vitro* data revealed that PEI/RBC-derived membranes' functionalization also improved the nanoparticles' cellular internalization and was capable of mitigating the hemolytic effects of AuMSS and AuMSS/PEI nanorods. In turn, the combinatorial chemo-photothermal therapy mediated by AuMSS/PEI/RBC_AO nanorods was able to completely eliminate HeLa cells, contrasting with the less efficient standalone therapies. Such data reinforce the potential of AuMSS nanomaterials to act simultaneously as photothermal and chemotherapeutic agents.

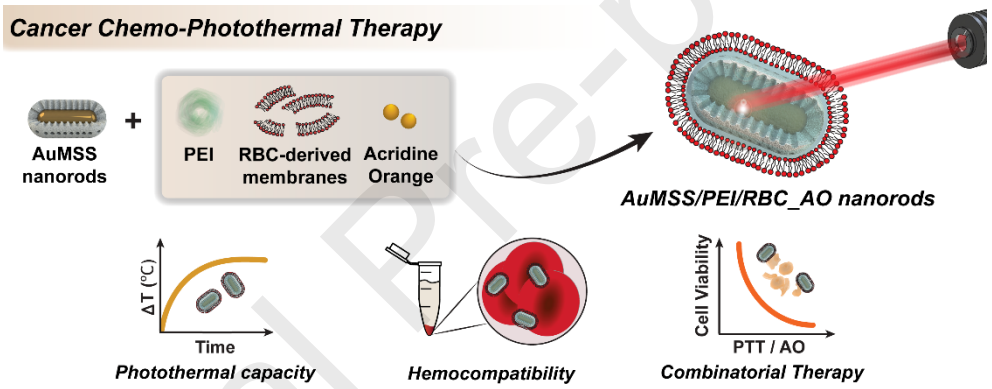

Keywords

Cancer, drug delivery, gold core silica shell nanorods, photothermal therapy, PEI, RBC-derived membranes.

List of Abbreviations

Abs: Absorbance

ANOVA: One-way analysis of variance

AO: Acridine orange

A.R.: Aspect ratio

AuMSS: Gold-core mesoporous silica shell

AuMSS/PEI: PEI functionalized AuMSS nanorods

AuMSS/PEI/HA_AO: AO-loaded AuMSS/PEI/HA nanorods

AuMSS/PEI/RBC: PEI and RBC-derived membranes functionalized AuMSS nanorods

BSA: Bovine serum albumin

CTAB: (1-Hexadecyl)trimethylammonium bromide

DMEM-F12: Dulbecco's modified eagle medium/nutrient mixture F-12

DMEM-HG: Dulbecco's modified eagle medium-high glucose

E.E.: Encapsulation efficiency

EPR: Enhanced permeability and retention

Ethanol: EtOH

FBS: Fetal bovine serum

FibH: Primary normal human dermal fibroblast

FITC: Fluorescein-5-isothiocyanate

FTIR: Fourier transform infrared spectroscopyHeLa: Cervical cancer cells

K-: Negative control

K- NIR: Cells non incubated with nanomaterials and irradiated

K+: Positive control

KRB: Krebs ringer buffer

NIR: Near-infrared

PBS: Phosphate buffered saline

PEI: Polyethylenimine

PEG: Polyethylene glycol

PFA: Paraformaldehyde

PTT: Photothermal therapy

RBC: Red blood cells

RES: reticuloendothelial system

s.d.: Standard deviation

TEM: Transmission electron microscopy

TEOS: Tetraethylorthosilicate

TESPIC: 3-(Triethoxysilyl)propyl isocyanate

THF: Tetrahydrofuran

WGA-Alexa Fluor® 594: Wheat germ agglutinin conjugate Alexa 594®

1. Introduction

The development and application of nanomaterials in medical research created new opportunities for cancer therapy (Gavas et al., 2021). Particularly, researchers have been actively investigating nanomaterials that can combine multiple therapeutic approaches to minimize off-target side effects and enhance the anti-tumoral response, overcoming cancer cells' resistance mechanisms (Al-Lazikani et al., 2012; Shrestha et al., 2019). The conjugation of chemotherapy with photothermal therapy (PTT) has rapidly grown as one of the most explored combinatorial therapeutic approaches for cancer (Khafaji et al., 2019; Li et al., 2019). This combinatorial approach takes advantage of the nanomaterials' capacity to improve drug solubility, protect drugs from premature degradation, and minimize drugs interaction with healthy tissues. The heat generated in response to external stimuli *i.e.,* near-infrared light (NIR; 700-1100 nm), improves blood flow, which consequently increases the nanoparticles accumulation in tumor tissue and maximize the benefits of drug delivery systems (de Melo-Diogo et al., 2019; de Melo-Diogo et al., 2017; Khafaji et al., 2019; Nam et al., 2018). Moreover, this localized tumor hyperthermia can sensitize the cancer cells to other therapeutic modalities, such as chemotherapy, or induce cellular damage that ultimately leads to the cancer cells death (Fernandes et al., 2020; Kang et al., 2020; Nam et al., 2018; Oei et al., 2015).

Until now, several materials, such as those made of gold have been explored to mediate a photothermal effect (Alves et al., 2022; de Melo-Diogo et al., 2019; Gonçalves et al., 2020). Among them, gold core silica shell (AuMSS) nanoparticles, particularly the rod-shaped AuMSS nanoparticles, emerged as one of the most explored cancer nanomedicines, due to their tunable optical properties, effective light-heat conversion, and drug delivery potential (Kennedy et al., 2011; Moreira et al., 2018a; Moreira et al., 2018b; Rodrigues et al., 2019a). This anisotropic gold core morphology confers to AuMSS nanomaterials' high absorption in the NIR region, which enables their application as photothermal agents. Moreover, AuMSS nanorods can also act as contrast agents in imaging modalities (*e.g.,* computed tomography and magnetic resonance imaging) due to the gold core' high mass attenuation (Dias et al., 2016; Luo et al., 2021; Moreira et al., 2018a; Rodrigues et al., 2019a). Additionally, the silica shell presents a large surface area, which can be easily functionalized with different moieties, and a mesoporous structure that allows the encapsulation of several therapeutic molecules (Moreira et al., 2018b; Rodrigues et al., 2021; Rodrigues et al., 2019a; Zhou et al., 2018). Overall, AuMSS nanorods can act as multifunctional nanomedicines with the potential to combine simultaneously their chemotherapeutic, PTT, and bioimaging capabilities.

Nevertheless, despite several pre-clinical studies showing the capacity of nanomaterials to detect, deliver, and induce cancer cells' death, their translation to clinical practice presents major obstacles (Rodrigues et al., 2022; Zhang et al., 2019). The administration of nanomedicines is generally performed through the intravenous route, and it is reported that less than 1% of nanoparticles' administered dose reaches the tumor tissue (Wilhelm et al., 2016). Indeed, after administration, nanomedicines can be highly susceptible to the adsorption of plasma proteins on their surface. This phenomenon can induce several modifications in nanoparticles' physicochemical properties, leading to increased immune recognition and accumulation in off-target tissues, which consequently reduces their blood retention and bioavailability (Corbo et al., 2016; Mahmoudi et al., 2016; Rodrigues et al., 2022).

For years, the primary strategy to improve nanoparticles' pharmacokinetic profile involved surface functionalization with hydrophilic polymers, such as polyethylene glycol (PEG) and poly-2-oxazolines, known for their anti-fouling properties and biocompatibility (Moreira et al., 2018b; Qi et al., 2019; Rodrigues et al., 2022; Sedlacek and Hoogenboom, 2020; Suk et al., 2016). However, different authors have described that multiple administrations of hydrophilic polymers, such as PEG, can elicit antibody responses and lead to an accelerated blood clearance phenomenon (Mima et al., 2015; Perry et al., 2012; Wang et al., 2019). With this in mind, biomimetic strategies based on cell-derived vesicles have gained huge attention to improve the nanomaterials' biological performance (Rodrigues et al., 2022). These cell-derived vesicles, including those from red blood cells (RBC), platelets, cancer, and immune cells, inherit the characteristics of their source cells, such as biocompatibility, extended circulation time, and immune evasion, making them highly promising for developing more effective cancer therapies (Jin and Bhujwalla, 2020; Rodrigues et al., 2022).

In this work, AuMSS nanorods functionalized with branched polyethylenimine (PEI) and red blood cells (RBC)-derived membranes, loaded with acridine orange (AO) were developed in order to be applied in cancer chemo-photothermal therapy. PEI is a cationic polymer that in acidic environments (*e.g.,* tumor tissue) can be easily protonated promoting the nanomaterials' interaction with cells and enhancing the nanomaterials' escape from lysosomes and/or endocytic vesicles (Rodrigues et al., 2019b; Vermeulen et al., 2018; Zakeri et al., 2018). On the other hand, RBC are nature's long-circulating delivery vehicles that have inspired the design of synthetic drug delivery systems (Xia et al., 2019; Ye et al., 2019). The obtained RBC-derived membranes can preserve some of the original surface markers of the source cells, such as CD47, which acts as a "don't eat me" marker and plays a significant role in reducing reticuloendothelial system (RES) uptake. Therefore, nanomaterials coated with RBC-derived membranes should be less susceptible to interaction with blood components, immune recognition, and premature clearance (Rodrigues et al., 2022; Xia et al., 2019). The functionalization of the AuMSS nanorods' surface was achieved through the condensation of a PEI-silane derivative, followed by the adsorption onto RBC-derived membranes. The results revealed that RBC-derived membranes increased the nanoparticles' hemocompatibility and stability. Additionally, PEI/RBC-derived membrane functionalization improved nanoparticles' cellular internalization and the combinatorial therapeutic effect toward cervical HeLa cancer cells.

2. Materials and Methods

2.1. Materials

Primary normal human dermal fibroblast (FibH) cells and cervical carcinoma (HeLa) cells were acquired from Promocell (Heidelberg, Germany) and ATCC (Middlesex, UK), respectively. (1-Hexadecyl)trimethylammonium bromide (CTAB, purity 98%),

Chloroauric acid ($HAuCl_4$, purity 99.9% metal basis, Au 49%, Mw: 339.77 g/mol), and 3-(triethoxysilyl)propyl isocyanate (TESPIC, purity 95%) were purchased from Alfa Aesar (Kandel, Germany). Hydrochloric acid (HCl), phosphoric acid, methanol, and coomassie brilliant blue G-250 were obtained from Fisher Scientific (Lisboa, Portugal). Tetraethylorthosilicate (TEOS, purity > 97%) and tetrahydrofuran (THF) were acquired from Acros Organics (Geel, Belgium), whereas acridine orange hydrochloride (AO) (purity > 98%) was obtained from Carbosynth (Berkshire, UK). PEI (Branched, Mw ~1250 g/mol), silver nitrate ($AgNO_3$), L-ascorbic acid, ethanol (EtOH, 33%, 95%, or 99.9% v/v), fluorescein 5-isothiocyanate (FITC), sodium borohydride ($NaBH_4$), paraformaldehyde (PFA), Dulbecco's Modified Eagle Medium/Nutrient Mixture F-12 (DMEM-F12), Dulbecco's Modified Eagle medium-high glucose (DMEM-HG), resazurin, and trypsin were obtained from Sigma-Aldrich (Sintra, Portugal). Bovine Serum Albumin (BSA) was obtained from Amresco (Pennsylvania, EUA). Fetal bovine serum (FBS) was purchased from Biochrom AG (Berlin, Germany), and cell imaging plates were bought from Ibidi GmbH (Munich, Germany). Propidium iodide (PI), Calcein-AM, Hoechst 33342®, wheat germ agglutinin conjugate Alexa 594® (WGA-Alexa Fluor® 594), and cell culture t-flasks were obtained from Thermo Fisher Scientific (Porto, Portugal). The filtered and double-deionized water used in all experimental procedures was obtained through a Milli-Q Advantage A10 Ultrapure Water Purification System (0.22 µm; 18.2 MΩ cm^{-1} at 25°C).

2.2. Methods

2.2.1. Synthesis of AuMSS nanorods

Gold nanorods were produced through a two-step seed-mediated methodology as described in the literature (Dias et al., 2016; Moreira et al., 2018b). First, $NaBH_4$ (0.01 M) was added to a solution containing 5 mL of CTAB (0.20 M) and 5 mL of $HAuCl_4$ (0.0005 M) and left at 30°C for 6 h, to promote the formation of small gold nanospheres (seeds). After this time, the seeds solution was added to a "growth solution" containing 200 mL of CTAB (0.2 M), 1.50 mL of $HAuCl_4$ (0.05 M), 150 µL of $AgNO_3$ (0.1 M), 1 mL of L-ascorbic acid (0.08 M), and left to react overnight at 30°C. Then, the obtained gold nanorods were recovered by centrifugation (12000 g, 20 min at 25°C) to allow the removal of CTAB in excess and resuspended in ultrapure water.

Afterward, the gold nanorods were coated with a mesoporous silica shell through Stöber method derivations (Dias et al., 2016; Gorelikov and Matsuura, 2008). Briefly, gold nanorods were added to a solution containing CTAB (0.01 M) and NaOH (0.1 M), and left under stirred for 30 min, at 40°C. Afterward, to promote the formation of mesoporous silica shell were added to the solution three injections of TEOS (0.03 mL, 20% v/v in methanol) with 30 min intervals, and left to react for 24 h.

Then, the produced AuMSS nanorods were recovered by centrifugation (12000 g for 20 min at 25°C) with posterior removal of the cytotoxic CTAB surfactant. For that purpose, AuMSS suffered several washing cycles (incubation and sonication) with an HCl solution (7.5% v/v in EtOH), followed by two washing steps with EtOH (99.9%) and ultrapure water. In all washing steps, AuMSS nanorods were recovered through centrifugation (18000 g, 20 min at 25°C) and stored at 4ºC.

2.2.2. Synthesis of PEI derivative silane

To promote the AuMSS surface functionalization with branched PEI, the cationic polymer was previously modified with TESPIC, as previously described by Rodrigues *et al.* (Rodrigues et al., 2021; Rodrigues et al., 2019b). For that purpose, the silane-modified PEI was produced through a hydrogen-transfer nucleophilic addition reaction between the amine groups of PEI and isocyanate groups of TESPIC. Briefly, PEI (0.2 mL) was

dissolved in 60 mL of dried THF and left for 6 h under stirring and nitrogen atmosphere at room temperature. Then, TESPIC (0.1 mL) was added to the PEI solution and left to react for 24 h. Afterward, the THF was evaporated (Rotavap®R-215, Büchi, Switzerland) and the obtained silane-modified PEI was dialyzed and freeze-dried. Subsequently, Fourier transform infrared spectroscopy (FTIR) spectra were acquired to confirm the production of silane-modified PEI.

2.2.3. Preparation of RBC-derived membranes

The whole blood was collected from adult mice and centrifuged (500 g, 5 min at 4°C) to remove the plasma. After that, the sample was resuspended with ≈30 mL of NaCl (150 mM) until it reached the previous plasma level, followed by homogenization and centrifugation at the previous conditions, being this step was repeated 3 times. Then, the supernatant was removed, and the RBC were resuspended in 20 mL PBS (1X) at pH 7.4. After centrifugation (800 g, 5 min at 4°C), the resulting washed RBC were resuspended in ≈20 mL ice-cold PBS (1X) and centrifuged (800 g, 5 min at 4°C), this step was repeated 3 times. Then, RBC were resuspended in 20 mL of ice-cold PBS (0.25X), vortexed, added to an ice bath for 20 min, and centrifuged (1000 g, 5 min at 4°C) to promote the hemolysis through a hypotonic treatment. This procedure was repeated 2 times, as described in the literature (Gao et al., 2013; Ren et al., 2017). Then, several washing steps with 20 mL of ice-cold PBS (1X) were performed to guarantee the complete release and removal of hemoglobin and intracellular contents. Finally, the obtained RBC-derived membranes were resuspended in 5 mL of PBS (1X) and stored at 4ºC.

2.2.4. AuMSS nanorods functionalization with silane-modified PEI and RBC-derived membranes

The surface modification of AuMSS nanorods was accomplished by the chemical linkage of the silane-modified PEI followed by the adsorption of RBC-derived membranes (Figure 1). For that purpose, AuMSS nanorods (10 mg) were resuspended in EtOH (33% v/v in ultrapure water, pH 4) and sonicated for 10 min. Then, silane-modified PEI polymer was added in a proportion (m/m) of 1:2 to the nanorods solution and left under stirring for 24 h. After this time, the produced AuMSS/PEI nanorods were recovered by centrifugation (6000 g, 20 min at 25°C) and washed several times with ultrapure water to remove the unlinked polymeric chains (Rodrigues et al., 2021; Rodrigues et al., 2019b). Afterward, the AuMSS/PEI nanorods were entrapped on RBC-derived membranes. To accomplish that, RBC-derived membranes were sonicated for 5 min in a test tube using an ultrasonic bath at a frequency of 50 kHz and a power of 220 W (Auxilab, Spain). Then, 500 µL (1 mg/mL) of AuMSS/PEI nanoparticles were mixed with RBC-derived membranes prepared from 200 µL of whole blood, followed by sonication and vortex for 1 min. The obtained AuMSS/PEI/RBC nanoparticles were recovered by centrifugation (6000 g, 20 min at 25°C) and washed with ultrapure water to remove the excess of RBC-derived membranes.

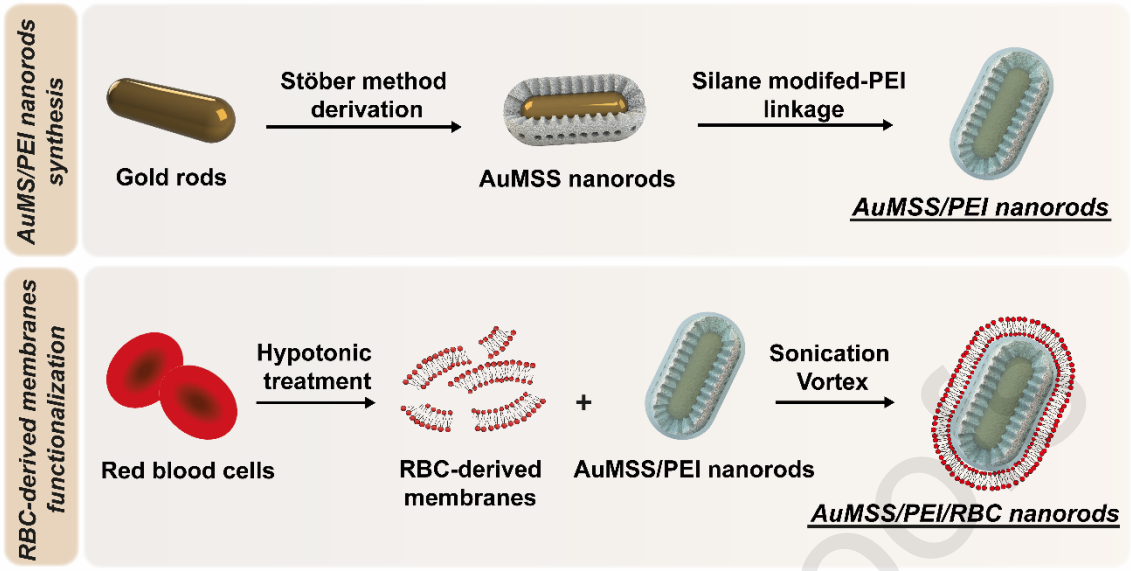

Figure 1. Schematic representation of AuMSS nanorods synthesis and functionalization with branched PEI polymer and RBC-derived membranes.

To produce AO loaded-AuMSS/PEI/RBC nanorods, AuMSS/PEI nanorods were resuspended in an AO solution (40 µg/mL in methanol), sonicated and then mixed with RBC-derived membranes, as previously described (Moreira et al., 2018b; Rodrigues et al., 2021). Then, AMSS/PEI/RBC_AO were recovered by centrifugation (18000 g, 20 min at 4°C), and the obtained supernatant was used to determine the concentration of AO loaded on AuMSS/PEI/RBC nanorods. Thus, the encapsulation efficiency (E.E) of AO was calculated by measuring the supernatant absorbance at 489 nm using an AO calibration curve (ABS=0.1981[AO]-0.0033; R^2=0.999) (Thermo Scientific Evolution 201 Bio UV-vis Spectrophotometer, Thermo Fisher Scientific Inc., USA).

$$E.E\ (\%) = \frac{(\text{Initial AO weight} - \text{AO weight in the supernatant})}{\text{Initial AO weight}} x100 \quad \textbf{(Equation 1)}$$

2.2.5. Physicochemical properties' characterization of AuMSS nanoformulations

AuMSS nanomaterials size and morphology were evaluated by Transmission electron microscopy (TEM; TECNAI G2 20 S-TWIN, EI Company, Amsterdam, The Netherlands). For that purpose, AuMSS nanoparticles were placed in formvar-coated copper grids and dried at room temperature. Then, TEM images were acquired at an accelerating voltage of 100 kV, and the AuMSS nanoformulations' overall size, rod core size, and mesoporous silica shell thickness were determined through ImageJ software measurements (ImageJ 2.0.0 NIH Image, USA), n=300. The successful production of AuMSS/PEI/RBC nanomaterials was confirmed through FTIR (4 cm^{-1} spectral resolution, from 600 to 4000 nm) using a Nicolet iS10 spectrometer (Thermo Scientific Inc. Massachusetts, USA). Additionally, the Energy-dispersive X-ray spectroscopic (EDX) analysis was performed to determine the elemental composition of the AuMSS nanoformulations and confirm their successful functionalization. For that purpose, AuMSS, AuMSS/PEI, and AuMSS/PEI/RBC nanorods samples were placed on aluminium stubs, air-dried at room temperature, and analyzed using an XFlash Detector 5010 (Bruker Nano, Germany), n=3. The AuMSS, AuMSS/PEI, and AuMSS/PEI/RBC nanomaterials' surface charge was measured using a Zetasizer Nano ZS equipment (Malvern Instruments, Worcestershire, United Kingdom). Also, AuMSS/PEI and AuMSS/PEI/RBC nanorods' preliminary stability studies were performed by monitoring zeta potential variations upon dispersion in phosphate-buffered saline (PBS; pH 5.6 or 7.4) for 26 h. Finally, the NIR light absorption capability of AuMSS and AuMSS/PEI/RBC nanomaterials was evaluated

through the acquisition of their UV-Vis-NIR spectrum (Thermo Scientific Evolution™ 201, ThermoFisher Scientific Inc, USA).

2.2.6. Evaluation of AuMSS nanoformulations' photothermal capacity

The *in vitro* photothermal capacity of AuMSS and AuMSS/PEI/RBC was evaluated using a thermocouple sensor (accuracy of 0.1ºC), as previously reported in the literature (Dias et al., 2016; Moreira et al., 2018b). Briefly, the AuMSS and AuMSS/PEI/RBC nanoformulations (at 200 µg/mL in PBS) were placed in 96-well flat-bottom culture plates (200 µL of total volume) and irradiated with a NIR laser (808 nm, 1.7 W/cm^2). Then, the temperature variations were registered from 1 to 10 min of irradiation. The temperature variation of a control group (PBS) without nanoparticles exposed to NIR laser was also monitored. Additionally, the photothermal conversion efficiency of both AuMSS and AuMSS/PEI/RBC nanorods was calculated as described in the literature (Gonçalves et al., 2022; Rodrigues et al., 2021).

2.2.7. *In vitro* drug release

The influence of pH and NIR laser irradiation on the AO release was evaluated as previously described in the literature (Rodrigues et al., 2021) (Moreira et al., 2020). For that purpose, AO-loaded AuMSS/PEI/RBC was resuspended in PBS at pH 5.6. or 7.4. and inserted in a Float-A-Lyzer dialysis bag. The dialysis was performed under magnetic stirring at 37ºC, for 48 h. Additionally, at 4 h of incubation, two groups were irradiated with NIR light (808 nm, 1.7 W/cm^2, 5 min). At predetermined time points, samples were collected, the dialysis bags were replaced with fresh PBS, and the released AO was quantified by the UV-Vis methodology, as previously described.

2.2.8. Cytocompatibility and hemocompatibility assays

The cytocompatibility of AuMSS nanoformulations was assessed on HeLa and FibH through the resazurin assay (Moreira et al., 2014). For that purpose cells were seeded in 96-well flat-bottom culture plates (10000 cells/well, 100 µL of DMEM-HG or DMEM-F12) and incubated in a humid atmosphere (37ºC, 5% CO_2) for 48 h. Afterward, the culture medium was removed and the cells were incubated with different concentrations (25 to 200 µg/mL) of AuMSS and AuMSS/PEI/RBC nanomaterials. After 24, 48, or 72 h of incubation, the cell viability was determined using the resazurin assay. Briefly, the culture medium was removed and a fresh culture medium containing 10% (v/v) of resazurin (1 mg/mL) was incubated in the dark at 37ºC for 4 h. Then, the fluorescence was measured at an excitation/emission wavelength of λ = 560 nm and λ = 590 nm with a Spectramax Gemini XS microwell plate reader (Molecular Devices LCC, CA, USA). Cells only incubated with cell culture medium were used as negative control (K-), whereas cells incubated with EtOH (99.9%) were used as positive control (K+).

Hemolysis experiments were also performed to evaluate the hemocompatibility of AuMSS nanoformulations (Moreira et al., 2018b; Rodrigues et al., 2021). For that purpose, EDTA-stabilized blood samples were obtained from adult mice, and the RBC were recovered. Briefly, the whole blood was centrifuged (500 g, 4ºC for 5 min) and then washed 3 times with a solution of NaCl (150 mM) and PBS. Subsequently, RBC were diluted in PBS, distributed to the test tubes, and centrifuged (500 g, 4ºC for 5 min). Different concentrations (50, 100, and 200 µg/mL in PBS) of AuMSS, AuMSS/PEI, and AuMSS/PEI/RBC nanomaterials were added to the obtained RBC suspension and incubated at room temperature for 4 and 24 h. RBC only incubated with PBS or Triton X-100 were used as negative (K-) and positive controls (K+), respectively. Then, the samples were centrifuged using the previous conditions and 100 µL of the supernatant

was transferred to a 96-well plate to quantify the hemoglobin absorbance (Abs) at 570 nm. Finally, the percentage of hemolysis was calculated through the following equation:

$$\text{Hemolysis (\%)} = \frac{\text{Sample Abs} - \text{K- Abs}}{\text{K+ Abs} - \text{K- Abs}} \times 100 \quad \textbf{(Equation 2)}$$

2.2.9. AuMSS nanoformulations' cellular internalization

The uptake of AuMSS nanoformulations by HeLa and FibH cells was also evaluated through fluorescence spectroscopy and confocal laser scanning microscopy (CLSM) (Moreira et al., 2018b; Rodrigues et al., 2021). To perform the fluorescence spectroscopy experiments, HeLa or FibH cells were seeded into 96-well flat-bottom culture plates (10000 cells/well, 100 µL of DMEM-HG or DMEM-F12) and incubated for 48 h in a humid atmosphere (37ºC, 5% CO_2). After this period, the culture media was removed and replaced with FITC-stained AuMSS or AuMSS/PEI/RBC nanomaterials at a concentration of 200 µg/mL. After 4 h of incubation, cells were washed with ice-cold Krebs Ringer Buffer (KRB) and lysed with Triton X-100 (1% in KRB, 30 min at 37°C). Cells only incubated with KRB were used as a negative control. Then, the FITC fluorescence was quantified using a spectrofluorometer (Spectramax Gemini XS, Molecular Devices LLC, CA, USA) at an excitation/emission wavelength of λex = 490 nm and λem = 520 nm.

Thereafter, CLSM images were acquired to confirm the nanoparticles' internalization capability by HeLa cells. To accomplish that, HeLa cells were seeded on µ-Slide 8 well Ibidi imaging plates (20000 cells/well, 200 µL of DMEM-HG) and incubated at 37°C. After 24 h, the medium was removed and cells were incubated with FITC-stained AuMSS and AuMSS/PEI/RBC nanoparticles (200 µg/mL) for 4 h. Afterward, cells were washed with PBS, fixed with PFA (4% w/v) for 10 min and rinsed again with PBS. Posteriorly, cells were treated with WGA-Alexa Flour® 594 for 30 min for the cytoplasm staining, and 20 min with Hoechst 33342® for the nucleus staining. CLSM experiments were performed on a confocal microscope (Zeiss LSM 710, Carl Zeiss SMT Inc., Jena, Germany) and the image analysis was performed in the Zeiss Zen 2012 software.

2.2.10. Evaluation of AuMSS nanoparticles *in vitro* therapeutic effect

2.2.10.1. AuMSS nanoparticles *in vitro* cytotoxic activity

The chemo-PTTcombinatorial effect of AuMSS/PEI/RBC nanomaterials was assessed on HeLa cells through the resazurin assay (Moreira et al., 2018b; Rodrigues et al., 2021). Briefly, HeLa cells were seeded in 96-well flat-bottom culture plates (10000 cells/well, 100 µL of DMEM-HG) and incubated for 48 h. Then, AuMSS nanorods (100 and 200 µg/mL) and AuMSS/PEI/RBC nanorods (100 and 200 µg/mL, with or without AO loaded) were incubated for 4 h. Afterward, cells were irradiated with a NIR laser (808 nm, 1.7 W/cm^2, for 5 min), and after 48 h of incubation, the cell viability was determined by resazurin assay, as described above. Cells cultured only with culture medium were used as negative control (K-), whereas cells incubated with EtOH (99.9%) were used as positive control (K+). Also, cells cultured only with culture medium and exposed to a NIR laser (808 nm, 1.7 W/cm^2, for 5 min) were used as NIR control (K NIR).

2.2.10.2. Live/dead assay

To further confirm the *in vitro* cytotoxic effect of AuMSS nanomaterials, the combinatorial therapeutic effect of AuMSS/PEI/RBC nanorods was characterized through the live/dead assay (Invitrogen, Life Technologies, CA, USA) (Jacinto et al., 2020). To accomplish that, HeLa cells were seeded on µ-Slide 8 well Ibidi imaging plates (20000 cells/well, 200

µL of DMEM-HG), and incubated at 37°C in a humid atmosphere (5% CO_2). After 24 h, the culture medium was removed and cells were incubated with AuMSS nanorods (200 µg/mL) and AuMSS/PEI/RBC nanorods (200 µg/mL, with or without AO loaded) for 4 h. After this period, cells were irradiation with a NIR laser (808 nm, 1.7 W/cm^2) for 5 min. Subsequently, HeLa cells were stained simultaneously with Calcein AM and PI (for 15 min) to allow the CLSM visualization of live and dead cells, respectively. The experiments were performed on a CLSM (Zeiss LSM 710) and the images were obtained in the Zeiss Zen 2012 software.

2.2.11. Statistical analysis

The obtained data are presented as the mean ± standard deviation (s.d.). The unpaired T-student test and one-way analysis of variance (ANOVA) (Student–Newman–Keuls post-test), were used to perform the statistical analysis of experiments with two groups and multiple group comparison, respectively. A p-value lower than 0.05 ($p < 0.05$) was considered statistically significant. Statistical analysis was performed using GraphPad Prism v.8.0 software (Trial version, GraphPad Software, CA, USA).

3. Results and Discussion

3.1. Synthesis and characterization of AuMSS nanoparticles

The rod-shaped AuMSS nanoparticles were synthesized through a seed-mediated methodology. This synthesis comprises three steps: i) production of small spheres (seeds); ii) growth of the seeds in the presence of ascorbic acid and silver nitrate to form the rod-like gold nucleus; and iii) nanorods coating with mesoporous silica in the presence of TEOS and CTAB micelles, serving as pore template (Dias et al., 2016; Rodrigues et al., 2019a). TEM images (Figure 2A and B) were used to confirm the successful synthesis of the AuMSS nanorods, revealing the organization in a single gold nanorod core coated with a uniform and homogeneous silica shell. Moreover, ImageJ measurements also show that the gold core has a length and width of 46 ± 8 and 15 ± 3 nm, respectively. These dimensions result in an aspect ratio (A.R.) of approximately 3.1, consistent with reported methodologies in the literature and within the 3 to 5 range, rendering it suitable for NIR-mediated PTT applications (Abadeer et al., 2014; Jacinto et al., 2020; Taylor et al., 2022; Wang et al., 2015). Additionally, the mesoporous silica shell presented a mean thickness of 21 ± 2 nm, resulting in a final AuMSS length and width of 85 ± 8 and 61 ± 5 nm, respectively. Therefore, this size range allows the AuMSS nanorods to take advantage of the tumor vascular fenestra and consequently promote their passive accumulation in the tumor tissue (*i.e.,* the enhanced permeability and retention effect) (de Melo-Diogo et al., 2017; Rodrigues et al., 2020).

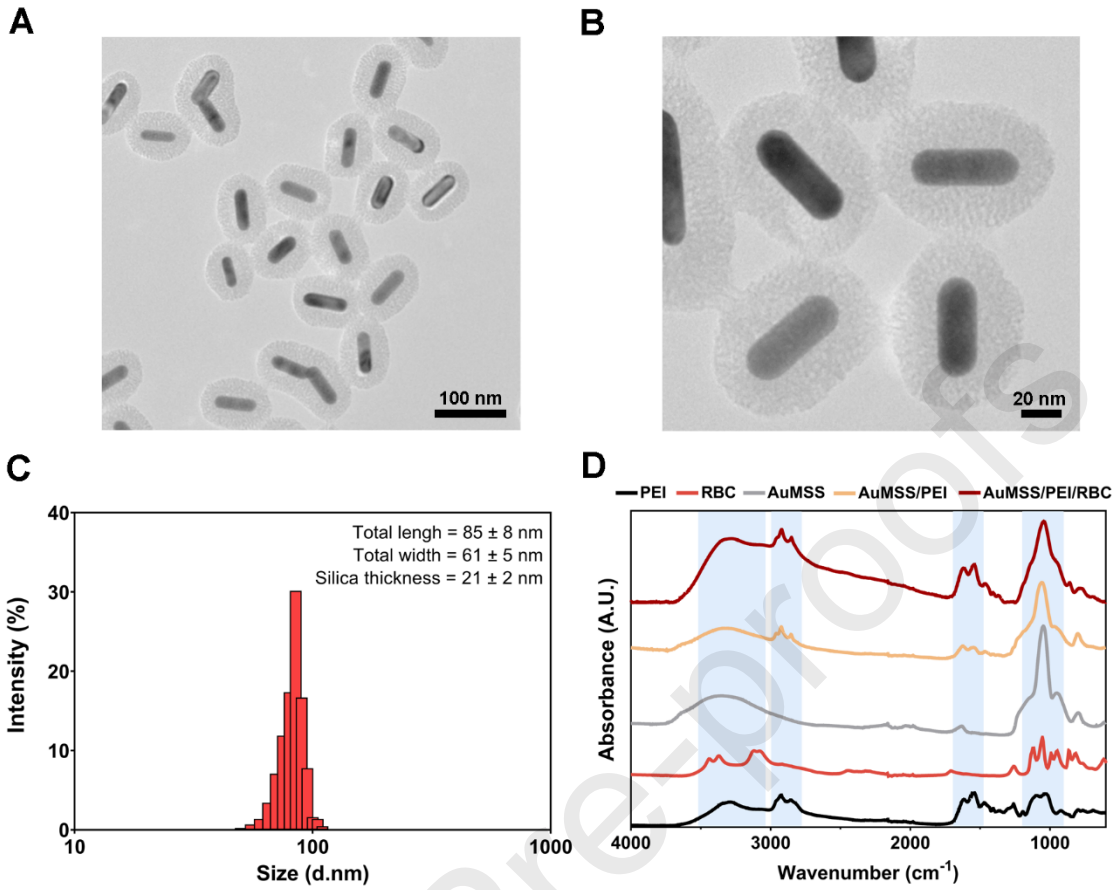

Figure 2. Physicochemical characterization of AuMSS nanomaterials. (A) and (B) TEM images of AuMSS nanorods at different magnifications. (C) Size distribution of AuMSS nanorods, including length and width, n=300. (D) FTIR spectra of AuMSS nanoformulations, silane-modified PEI polymer, and RBC-derived membranes.

FTIR analysis of the AuMSS nanorods (Figure 2D) presents the three characteristic peaks of the mesoporous silica shell in the 1100–750 cm^{-1} region, corresponding to Si–O, Si-OH, and Si–O–Si vibrations. Besides confirming the successful formation of the mesoporous silica coating, the FTIR spectrum also demonstrates the effective removal of the cytotoxic surfactant CTAB from the nanoparticles. Specifically, the two characteristic bands of CTAB at 2950–2850 cm^{-1} (C-H vibration) and at 1450-1500 cm^{-1} (CH_3-N^+ deformation) are not observed in the AuMSS nanorods spectrum (Dias et al., 2016; Su et al., 2015).

After confirming the production of AuMSS nanorods, surface modification with PEI and RBC-derived vesicles was achieved by two different steps: i) functionalization with the silane-modified PEI polymer, followed by ii) modification with RBC-derived membranes (Figure 1). In the first approach, the silane-modified PEI was obtained by promoting the TESPIC linkage to the PEI backbone through a hydrogen-transfer nucleophilic addition reaction. Such promotes the reaction between the isocyanate groups of TESPIC and amine groups of PEI, as previously demonstrated by Rodrigues and co-workers (Rodrigues et al., 2021; Rodrigues et al., 2019b). Then, the silane-derivative of PEI was grafted on AuMSS nanorods' surface through a condensation reaction (Rodrigues et al., 2019b). Subsequently, to promote the final modification with RBC-derived vesicles, RBC were isolated from mouse whole blood. The recovered RBC were then hemolyzed through a hypotonic treatment and washed to obtain the RBC-derived membranes (Gao et al., 2013; Ren et al., 2017). Then, AuMSS/PEI nanorods were mixed with RBC-derived

membranes sonicated, and vortexed to promote the reorganization of RBC-derived membranes, enclosing the AuMSS/PEI nanorods. This process is governed by the charge difference between AuMSS/PEI and RBC-derived membranes, leading to electrostatic interactions between the positively charged amine groups on PEI and the negatively charged groups of RBC-derived membranes.

The modification of AuMSS with the silane-modified PEI and RBC-derived membranes was confirmed through FTIR analysis (Figure 2D). The post-synthesis grafting of the silane-modified PEI onto the AuMSS nanorods was confirmed by the presence of peaks in the 1700-1400 cm^{-1} and 3000-2885 cm^{-1} regions, corresponding to N-H deformation and C-H stretching vibrations of PEI, respectively (Rodrigues et al., 2021; Rodrigues et al., 2019b). Furthermore, in comparison to uncoated AuMSS nanorods, AuMSS/PEI nanorods present an attenuation of the Si-OH peak at 950 cm^{-1}, indicating the grafting of the PEI-derivative through a condensation reaction (Moreira et al., 2018b; Rodrigues et al., 2021). The subsequent modification of nanoparticles with RBC-derived membranes resulted in the alteration of nanoparticles' spectra in the 3000-3200 cm^{-1} region, corresponding to the amide groups of the proteins present on RBC membranes. Also, the peaks on the 2830–2980 cm^{-1} region can be related to the RBC membranes' methyl and methylene hydrocarbon chains. Also, the attenuation of previous nanoparticles' peaks on 1280–1020 cm^{-1} and 1000–940 cm^{-1} regions are related to the phosphate and choline bands, respectively, that are related to phosphate groups present on the RBC membranes (Bebesi et al., 2022; Blat et al., 2019; Mazur et al., 2020). Additionally, the AuMSS, AuMSS/PEI, and AuMSS/PEI/RBC nanorods composition was also characterized through EDX analysis (Table S1 and S2) to further confirm the AuMSS nanorods functionalization with PEI and RBC-derived membranes. When compared to the AuMSS, it was possible to observe the presence of a new element, the nitrogen (N), in both AuMSS/PEI and AuMSS/PEI/RBC nanoformulations, which is related to the amine groups of PEI chains. Moreover, phosphor (P) is only present in AuMSS/PEI/RBC nanorods, which can be explained by the phosphate groups present in RBC-derived membranes. Altogether, the EDX results further corroborate the successful functionalization of AuMSS nanorods with PEI and RBC-derived membranes.

Further, the AuMSS nanorods functionalization was also confirmed by measuring the zeta potential of AuMSS nanoformulations (Figure 3A). The AuMSS nanorods have a negative surface charge of -26 ± 2 mV, attributed to the negative silanol groups on the mesoporous silica shell surface (Dias et al., 2016). On the other side, the AuMSS/PEI nanoparticles exhibited a highly positive surface charge of 42 ± 3 mV. This confirms the successful grafting of PEI on the AuMSS nanorods' surface, as branched PEI is rich in protonatable amine groups, imparting a cationic nature to the nanoparticles (Rodrigues et al., 2021; Zakeri et al., 2018). The subsequent modification of nanoparticles with RBC-derived membranes led to a decrease and neutralization of the nanoparticle's surface charge to -16 ± 2 mV, which is in agreement with the negative surface charge characteristic of RBC membranes (Ren et al., 2017). Comparing with AuMSS and AuMSS/PEI formulations, the surface charge value of AuMSS/PEI/RBC nanorods is closer to the range considered ideal for the nanomaterials' circulation in the bloodstream (± 10 mV). This can minimize the interaction of nanoparticles with the RES and, consequently, enhance blood circulation time (de Melo-Diogo et al., 2017; Rodrigues et al., 2020). Simultaneously, the stability of the PEI/RBC-derived membranes' modification was also evaluated by studying the changes in the nanomaterials' surface charge upon incubation in media at two different pH values, 7.4 (physiological conditions) and 5.6 (tumor microenvironment) (Figure 3B). The obtained results show that the incubation of AuMSS/PEI nanomaterials at pH 7.4 over time promotes a slight decrease in the surface charge from 45 to 35 mV. Additionally, upon acidification of the media (pH reduced to 5.6 between 24 h and 26 h), AuMSS/PEI nanoparticles exhibited an increase of the surface charge to 43 mV. In contrast, AuMSS/PEI/RBC nanomaterials maintained their

surface charge during the 24 h of incubation at pH 7.4 and presented a surface increase from -15 to -10 mV after the acidification of the medium to pH 5.6 between 24 h and 26 h of incubation. Therefore, these stability tests indicate that incubating nanoparticles in acidic pH led to the protonation of amine groups of PEI, and consequently to a slight increase in the surface charge of AuMSS/PEI and AuMSS/PEI/RBC nanoparticles. These results are in accordance with other reports where the nanoparticles functionalization with RBC-derived membranes results in the surface charge neutralization and stability for hours and/or days (Liu et al., 2018; Liu et al., 2023; Rao et al., 2015). For example, Ren *et al.* developed RBC-derived vesicle coated- albumin nanoparticles loaded with indocyanine green and perfluorocarbon for cancer photodynamic therapy. The authors observed that RBC-derived membranes inclusion resulted in a surface charge increase from -32 mV to -16 mV (Ren et al., 2017). Similarly, Wang *et al.* developed RBC-derived membranes to camouflage polypyrrole nanoparticles, reporting that RBC-derived membranes coating led to a reduction of nanoparticles surface charge from (-33 to -28 mV) with slight charge variations for 7 days. Moreover, it is worth noticing that these data demonstrate the success and stability of the AuMSS functionalization with PEI/RBC-derived membranes (Wang et al., 2017).

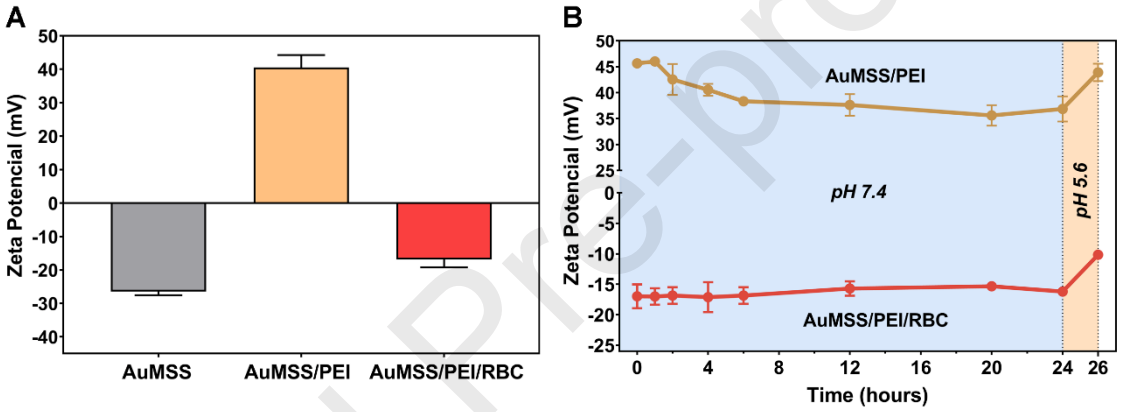

Figure 3. Characterization of nanoparticles' surface charge and stability. (A) Surface charge of AuMSS, AuMSS/PEI, and AuMSS/PEI/RBC nanorods. (B) Analysis of surface charge variation in AuMSS/PEI and AuMSS/PEI/RBC nanorods when dispersed in media at pH 7.4 for 24 h followed by acidification to 5.6 for 2 hours. Data are presented as mean ± s.d., n=3.

To assess whether the AuMSS functionalization process had an impact on the proteins present in RBC-derived membranes, the Bradford method was used to quantify the overall protein content in the samples (please see the method description in the Supporting Information). For that purpose, the protein content of RBC-derived membranes before and after the coating of AuMSS/PEI nanorods was determined through the utilization of a BSA calibration curve. The obtained results show a similar protein content in the samples obtained from RBC-derived membranes and AuMSS/PEI/RBC nanorods, 0.158 ± 0.008 and 0.123 ± 0.019 mg/mL, respectively. Such indicates that the method used for the functionalization of AuMSS/PEI nanorods has a minimal impact on the protein present in the RBC-derived membranes, which could lead to the loss of the desired bioactive properties.

Otherwise, during the functionalization with RBC-derived membranes, the encapsulation of AO, serving as a drug model, was also studied to further evaluate the potential of AuMSS/PEI/RBC nanorods to act as drug delivery agents for combinatorial chemo-photothermal therapy of cancer. For that purpose, AuMSS/PEI nanorods were resuspended in an AO solution (40 µg/mL) and then sonicated. After that, the solution was mixed with RBC-derived membranes to produce the AuMSS/PEI/RBC_AO nanorods, as described above. The results obtained revealed that AuMSS/PEI/RBC

nanorods could encapsulate AO, exhibiting an encapsulation efficiency of ≈40%, with 14 µg of AO per mg of AuMSS/PEI. Despite the encapsulation efficiency be lower than that reported in the literature, it is worth noting that in this work was used a sonication method, which allows the simultaneous loading of AO and entrapment of the AuMSS nanorods, instead of more laborious impregnation methods described in previous studies (Moreira et al., 2018b; Rodrigues et al., 2021; Rodrigues et al., 2019b). For example, Rodrigues *et al.* reported the AO loading in AuMSS/PEI nanoparticles through an impregnation method, with an encapsulation efficiency of 70% with 21 µg of AO per mg of particles (Rodrigues et al., 2021). However, in another study, an identical impregnation method was used to encapsulate AO on AuMSS and PEG/4-methoxybenzamide functionalized AuMSS nanospheres, where the encapsulation efficiency only reached 48 and 53%, respectively (Guimaraes et al., 2021).

3.2. *In vitro* evaluation AuMSS nanoparticles' photothermal potential and AO release profile.

The potential of AuMSS and AuMSS/PEI/RBC nanorods for being applied in photothermal therapy was initially evaluated by UV-vis-NIR spectroscopy (Figure 4B). The produced AuMSS and AuMSS/PEI/RBC nanorods exhibited two peaks, at ≈520 and ≈750 nm (within the NIR region), which correspond to the characteristic transverse and longitudinal plasmon resonances of gold nanorods, respectively (Shajari et al., 2017). Additionally, it was observed that PEI/RBC-derived membranes' functionalization induced a slight red-shift in the absorption peaks by ≈10 nm. Moreover, the longitudinal absorption peak obtained for the AuMSS nanoformulations aligns with what is expected from the gold nanorods' A.R. (3.1) and supports their application as NIR-triggered photothermal agents (Rodrigues et al., 2019a).

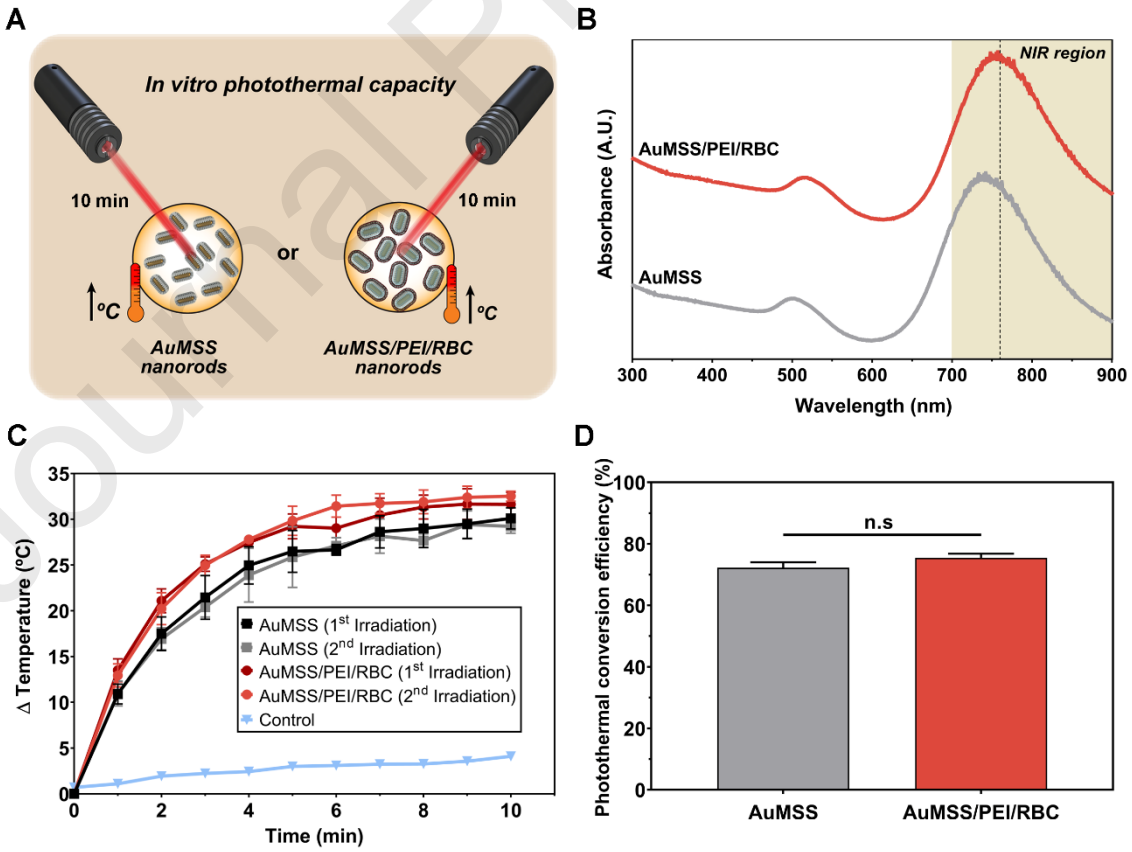

Figure 4. Evaluation of AuMSS nanoparticles photothermal potential. (A) Schematic representation of the evaluation of AuMSS nanoformulations *in vitro* PTT capacity. (B) UV-vis spectra of AuMSS and AuMSS/PEI/RBC nanorods. (C) Temperature variation curves of AuMSS and AuMSS/PEI/RBC nanorods when resuspended in PBS pH 7.4, under 1 or 2 NIR laser irradiation cycles (808 nm, 1.7 W/cm^2, 10 min). (D) Photothermal conversion efficiency of AuMSS and AuMSS/PEI/RBC nanorods. Data are presented as mean ± s.d., n=3.

Thereafter, the NIR light-to-heat conversion capacity of AuMSS nanoformulations was evaluated by measuring the temperature variation in response to NIR laser irradiation (Figure 4C). Both AuMSS nanoformulations mediated a ≈30°C temperature increase upon 10 min of NIR irradiation, resulting in photothermal conversion efficiencies of 72 and 75% for AuMSS and AuMSS/PEI/RBC nanorods, respectively (Figure 4D). These values are in agreement with data available in the literature for similar AuMSS nanorods and gold nanorod cores (Gonçalves et al., 2022; Gong et al., 2021; Rodrigues et al., 2021; Seo et al., 2022). Moreover, it is worth noticing that the AuMSS functionalization did not induce any significant changes in the AuMSS light-to-heat conversion capacity. Additionally, no significant differences in the registered temperatures were observed in the second irradiation cycle, demonstrating the photothermal stability of the gold nanorod core (Figure 4C). Altogether, these results demonstrate that both nanomaterials can induce localized hyperthermia (> 42ºC), highlighting the promising potential of AuMSS nanoformulations as PTT agents. Consequently, these AuMSS and AuMSS/PEI/RBC formulations hold the potential for mediating the cancer cells´ destruction or sensitizing them to the chemotherapeutics action, under NIR irradiation.

Finally, the release profile of AO from AuMSS/PEI/RBC nanorods was characterized at pH 5.6 (simulate the lysosomal compartments and tumor tissue) and pH 7.4 (simulate the physiological conditions), in the presence or absence of NIR laser irradiation. The obtained results (Figure S2) revealed that in the 48 h of the study, the AO presented a slightly faster release in acidic pH reaching a total of 53% of drug release at pH 5.6. In turn, the AuMSS/PEI/RBC group incubated at pH 7.4 presented a total drug release of 42%. Furthermore, NIR irradiation (808 nm, 1.7 W/cm^2, 5 min) of nanoparticles after 4 h of incubation further accelerated the drug release at both tested pH values. The AO release increased to 50 and 68% at pH 7.4 and 60 and 74% at pH 5.6, after 24 and 48 h of incubation, respectively. These results can be explained by the heat generation and consequent increase in the temperature of the media, which can enhance the AO solubility and even induce the disruption/disorganization of the RBC-derived membranes' coating, facilitating the AO release from AuMSS/PEI/RBC nanorods.

Comparing these results with our previous reports with bare AuMSS nanorods, it was possible to observe that AuMSS/PEI/RBC nanorods induced a more sustained and controlled drug release, which is attributed to the additional barrier provided by the PEI/RBC functionalization. For example, Rodrigues *et a*l, reported that bare AuMSS nanorods release 80% of the AO content when incubated at pH 7.4 and 5.6 for 48 h. In contrast, surface-modified AuMSS/PEI/HA nanorods promoted a slower AO release, with 42 and 49% of AO release at pH 7.4 and 5.6, respectively (Rodrigues et al., 2021). Altogether, the more controlled AO release presented a huge relevance, since it can prevent the premature and burst release of AO from the nanomaterial, and consequently minimize the drug off-target interactions during blood circulation. Furthermore, the enhanced release profile under NIR irradiation and pH 5.6 may improve the AO release from AuMSS/PEI/RBC nanoparticles in the tumor tissue and consequently improve the cancer chemo-PTT effect.

3.3. Evaluation of nanoparticles' biocompatibility

3.3.1. Characterization of nanoparticles' cytocompatibility

The biocompatibility of AuMSS and AuMSS/PEI/RBC nanorods was assessed on HeLa and FibH cells. Test concentrations ranging from 25 to 200 µg/mL were incubated for 24, 48, and 72 h with HeLa or FibH cells, and the cell viability was quantified through the resazurin assay. The results revealed that AuMSS and AuMSS/PEI/RBC nanoparticles, at concentrations up to 200 µg/mL, remained biocompatible for both cell lines, with cell viabilities close to 100% throughout the 72 h study period (Figure 5). These data are in agreement with the previous reports available in the literature, where AuMSS nanorods present good cytocompatibility within the concentration range of 25 to 200 µg/mL (Dias et al., 2016; Hu and Gao, 2011; Moreira et al., 2018b). Nevertheless, our previous work revealed that AuMSS functionalization with PEI induces a dose-dependent variation in cell viability, attributed to the high positive charge of PEI chains that induce the cells death (Rodrigues et al., 2019b). In turn, our data demonstrate that the final modification with RBC-derived membranes addresses the toxicity triggered by PEI, resulting in biocompatible nanomaterials. These results are in accordance with AuMSS/PEI/RBC surface charge (-16 mV), as well as with the literature reports for the biocompatibility of RBC-derived membranes and AuMSS nanoparticles' functionalization with hydrophilic polymers (*e.g.,* hyaluronic acid, d-α-Tocopheryl polyethylene glycol 1000 succinate (TPGS), poly-2-oxazolines) (Jacinto et al., 2020; Moreira et al., 2018b; Rodrigues et al., 2021).

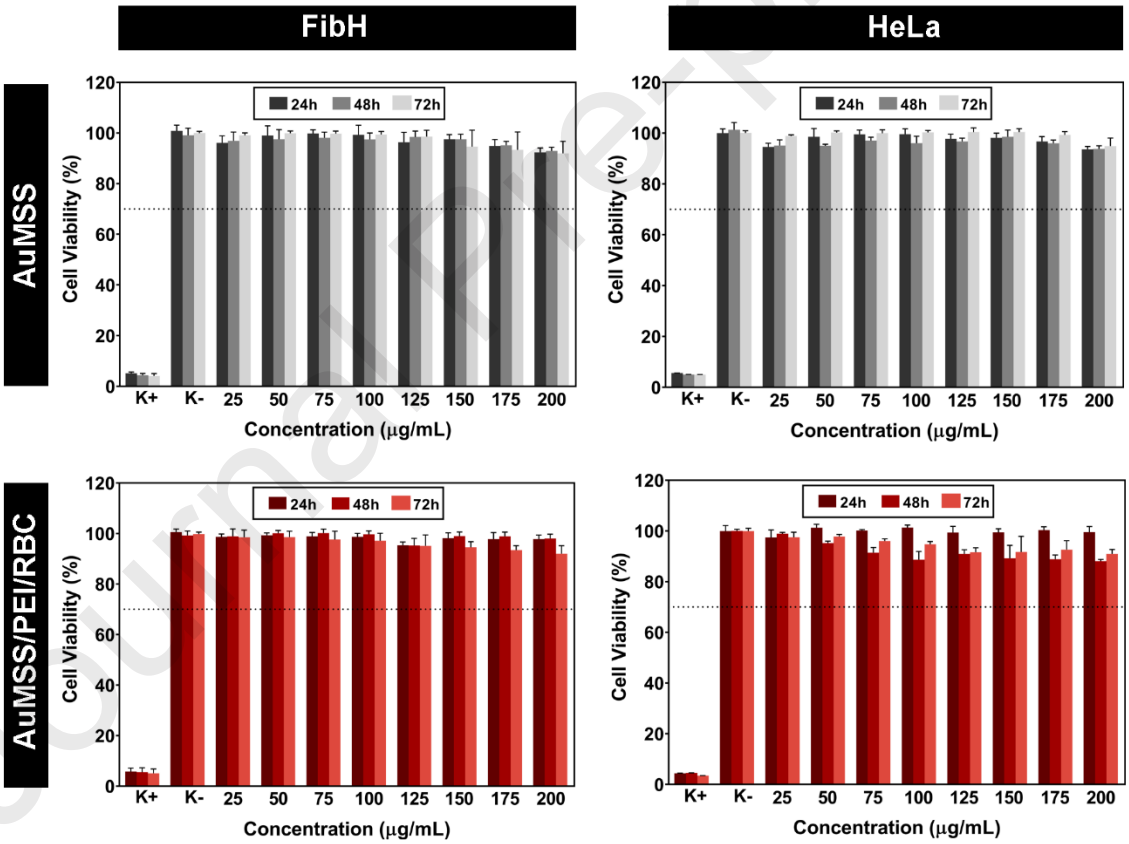

Figure 5 - Evaluation of AuMSS and AuMSS/PEI/RBC nanorods cytocompatibility in FibH and HeLa cells at 24, 48, and 72 h. Positive control (K+): cells treated with EtOH. Negative control (K-): cells without being incubated with nanoparticles. Data are presented as mean ± s.d., n=5.

3.3.2. Nanoparticles' hemocompatibility

Hemocompatibility studies were conducted to further characterize the biosafety of AuMSS nanoformulations, upon incubation with RBC for 4 and 24 h (Figure 6). The obtained results show a dose dependent hemolytic effect for both AuMSS and AuMSS/PEI nanorods, with hemolysis increasing with concentration. In fact, the PEI

functionalization further increased the hemolysis registered with the nanomaterials' incubation, from 2.5% to 3.2% at 4 h and from 5% to 8.9% at 24 h of incubation, at a concentration of 200 µg/mL. These data are in agreement with the results previously attained for AuMSS nanorods functionalized with PEI and can be explained by the higher surface charge of AuMSS/PEI nanoparticles (> 40 mV), resulting in cell membrane' destabilization and hemolysis (Rodrigues et al., 2021; Rodrigues et al., 2019b). For example, Rodrigues *et al*, developed AuMSS nanorods functionalized with PEI and HA, and was reported that PEI grafting on the AuMSS nanorods exacerbated the hemolysis at all time points and tested concentrations (Rodrigues et al., 2021). However, the posterior HA complexation was able to mask this effect and reduce the hemolysis to safe values.

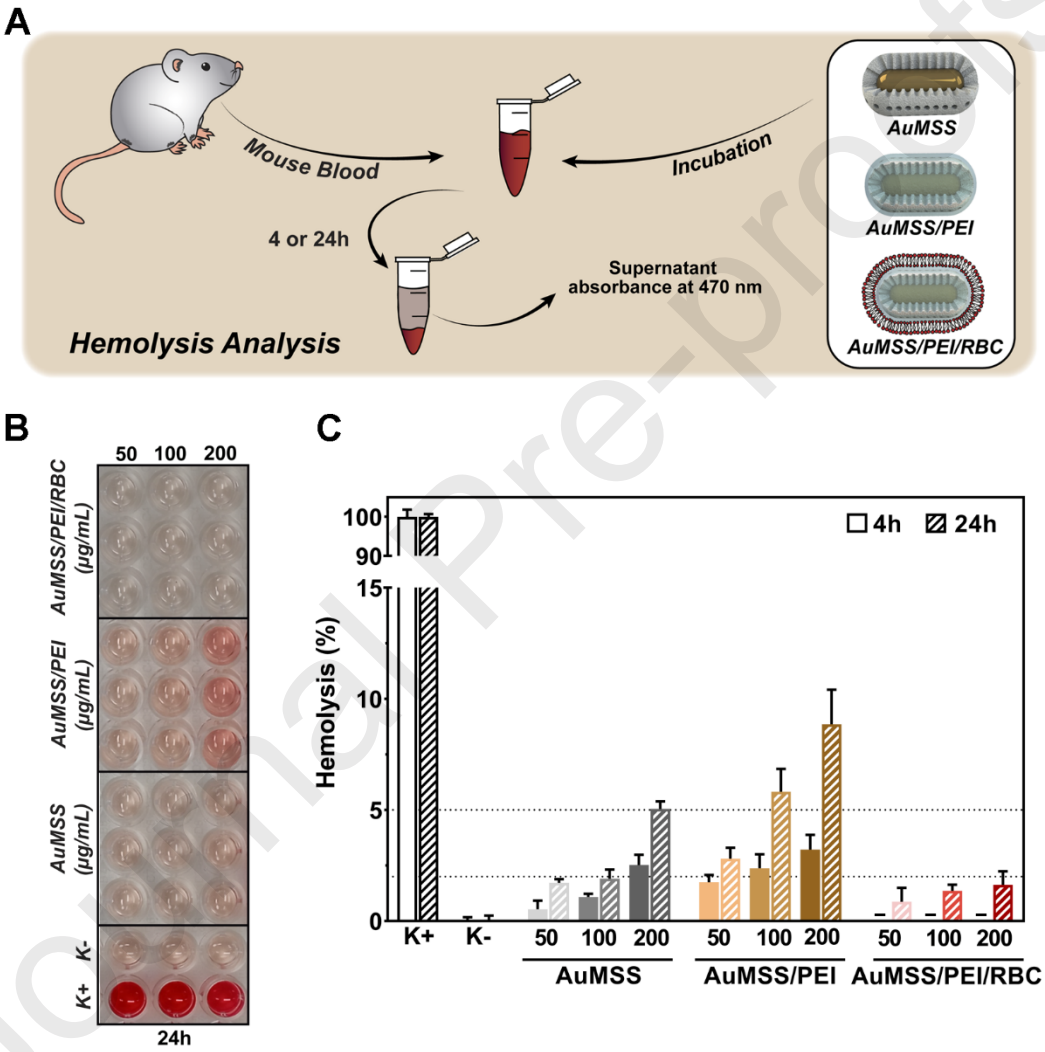

Figure 6 - Evaluation of AuMSS nanoformulations hemocompatibility. (A) Schematic representation of the methodology used to perfomed the hemocompatibility study. (B) Optical images of blood supernatants after 24 h of incubation with AuMSS, AuMSS/PEI, and AuMSS/PEI/RBC nanomaterials. (C) Analysis of RBC lysis upon incubation with different concentrations (50, 100, and 200 µg/mL) of AuMSS nanoformulations. RBC only incubated with PBS or Triton X-100 were used as negative (K-) and positive controls (K+), respectively.

Our data also demonstrate that RBC-derived membranes enhance the hemocompatibility of AuMSS nanorods, with ≈0% of hemolysis registered after 4 h of incubation, even for the highest concentration tested. Moreover, at 24 h of incubation, hemolysis values remained at ≈1% for all tested concentrations, demonstrating the non-hemolytic nature of AuMSS/PEI/RBC nanorods. These results can be attributed to the

neutralization of the surface charge to safer values, *i.e.,* -16 mV, which reduces the nanoparticles' interaction with blood cells. Overall, these results align with previous reports on AuMSS nanomedicines, as well as the biocompatibility of RBC-derived membranes and their reduced interaction with blood components (Jacinto et al., 2020; Liu et al., 2019; Reis et al., 2019; Xia et al., 2019). Additionally, these findings are consistent with guidelines established by international agencies for critically safe hemolytic ratios (ISO/TR 7406), moderate hemolytic materials if hemolysis between 2 and 5% and hemolytic materials if hemolysis ≥ 5%.

3.4. Evaluation of AuMSS nanomaterials cellular internalization

The uptake of AuMSS and AuMSS/PEI/RBC nanorods by cancer cells was evaluated through fluorescence spectroscopy and CLSM to assess the nanoparticles' capacity to overcome the final barrier to the delivery of therapeutics (Figure 7A). For that purpose, the uptake of FITC-stained AuMSS and AuMSS/PEI/RBC nanorods was evaluated and quantified by fluorescence spectroscopy after incubation for 4 h with HeLa or FibH (Figure 7B). The results demonstrated that FITC-stained AuMSS/PEI/RBC nanoparticles presented ≈2 times higher uptake in both cells lines than those treated with AuMSS nanorods. These results indicate that AuMSS surface charge neutralization (*i.e.,* -26 mV to -16 mV after the PEI/RBC-derived membranes coating) can favor the nanoparticles' interaction with cell membranes and increase cellular uptake. Moreover, RBC-derived membranes are known for their camouflage effect, extending circulation time through the expression of CD47—a 'don't eat me' signal to immune cells. However, it is important to note that these membranes inherently lack the capacity for targeting cancer cells (Rodrigues et al., 2022; Xia et al., 2019). Such is in accordance with our data, with the AuMSS/PEI/RBC nanorods showing no preference between the healthy (FibH) and cancer cells (HeLa).

Additionally, CLSM images (Figure 7C) show that all nanoformulations (identified with the white arrows) can be successfully internalized by HeLa cells. However, in these images, AuMSS/PEI/RBC nanoparticles exhibit a seemingly higher degree of cellular internalization in HeLa cells compared to the uncoated AuMSS nanorods. This also supports the understanding that the PEI/RBC-derived membranes can accelerate the internalization of AuMSS nanorods. This, in turn, facilitates drug release in the cell cytoplasm, preventing premature drug degradation and enhancing the therapeutic potential of the nanomedicines.

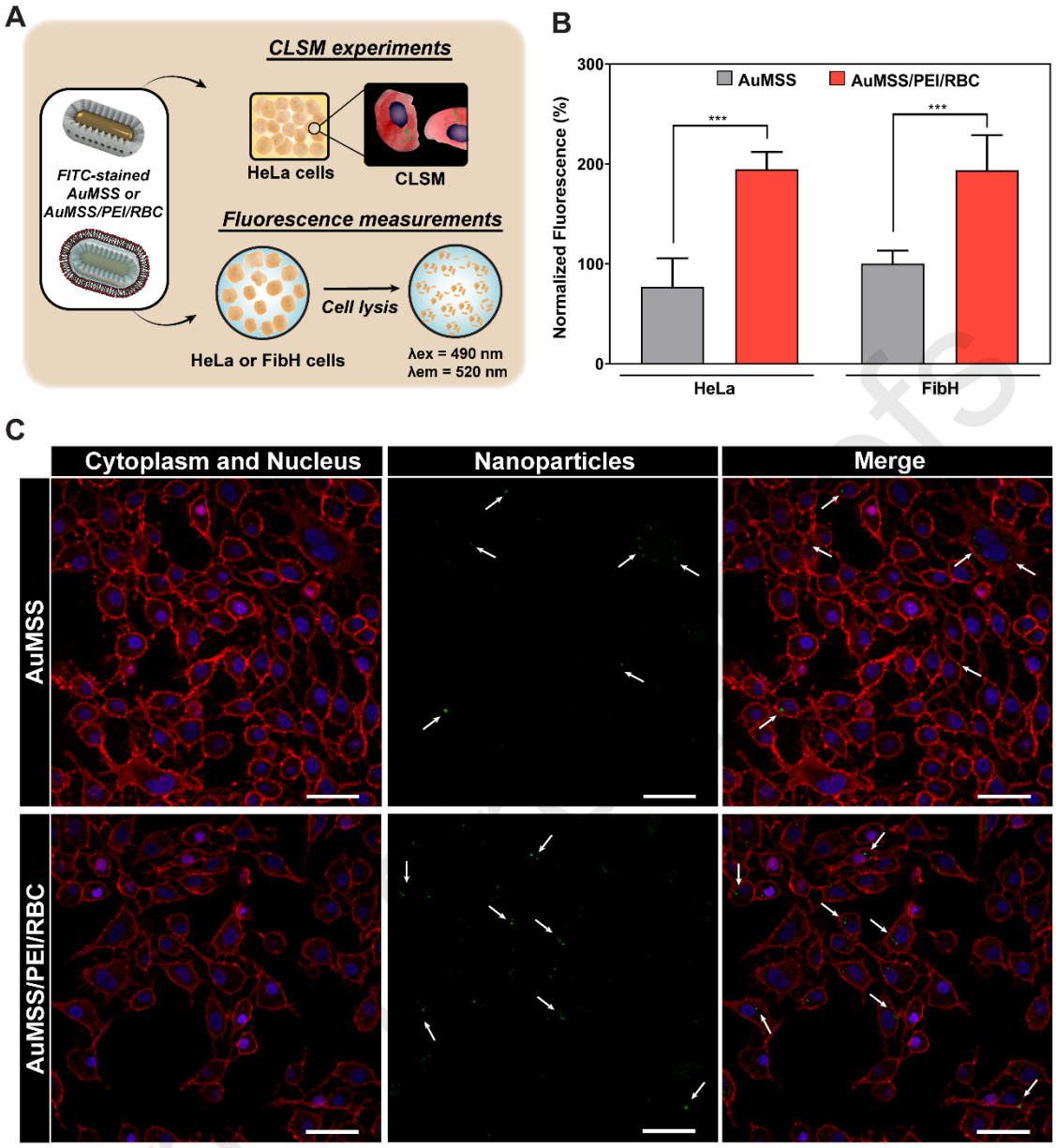

Figure 7 - Evaluation of the AuMSS nanomaterials' uptake by FibH and HeLa cells after 4 h of incubation. (A) Schematic representation of the uptake experiments of AuMSS nanomaterials. (B) Fluorescence spectroscopy analysis of the uptake of AuMSS and AuMSS/PEI/RBC nanorods by FibH and HeLa cells, normalized to the AuMSS nanorods-treated groups. Data are presented as mean ± s.d., (***$p < 0.001$), n=5. (C) CLSM images of the FITC-stained AuMSS nanoformulations' uptake by HeLa cells, white arrows are pointing to the internalized nanoparticles. Scale bar = 50 µm. Blue channel: Hoechst 33342® - stained cell nucleus; WGA-Alexa Fluor 594® - stained cell cytoplasm; Green channel: FITC - stained AuMSS nanoformulations.

3.5. Evaluation of AuMSS nanomaterials' therapeutic effect

After confirming the biocompatibility and internalization capability of the nanomaterials, the chemo-PTT anticancer potential of AuMSS/PEI/RBC_AO nanomaterials was evaluated using HeLa cells (Figure 8A). For that purpose, HeLa cells were incubated for 48 h with different concentrations (100 and 200 µg/mL) of AuMSS, AuMSS/PEI/RBC, and AuMSS/PEI/RBC_AO nanorods, with or without NIR laser irradiation (808 nm, 1.7 W/cm^2, for 5 min). In Figure 8B, it can be observed that both AuMSS and AuMSS/PEI/RBC nanoformulations, in both single or combined therapies, mediate a dose-dependent decrease in HeLa cells' viability. The single therapies mediated by the

AuMSS/PEI/RBC nanorods, at a concentration of 100 µg/mL, reached cell viabilities of 55% and 83% for single PTT and AO delivery, respectively. These therapeutic results further increased when a higher concentration (200 µg/mL) was used, reaching a final cellular viability of 9% and 63% for single PTT and AO delivery, respectively. In turn, the combinatorial therapy mediated by AuMSS/PEI/RBC nanorods resulted in a 59% and 95% reduction in HeLa cells viability for the group treated with 100 and 200 µg/mL, respectively.

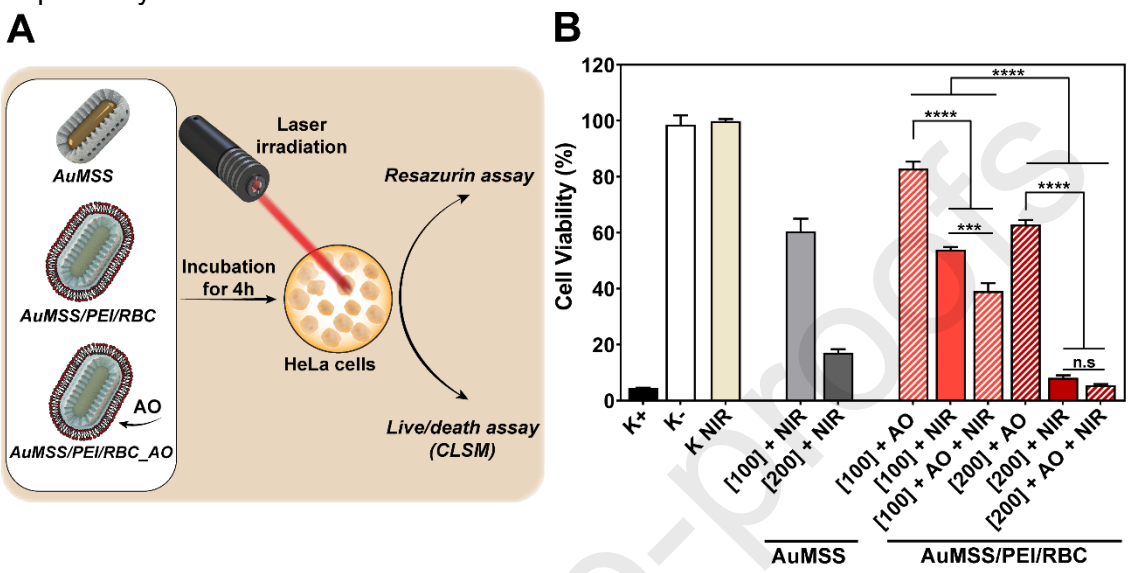

Figure 8- Evaluation of the therapeutic potential of AuMSS formulations in HeLa cancer cells. (A) Schematic representation of cytotoxic experiments with AuMSS nanomaterials under NIR laser irradiation (808 nm, 1.7 W/cm^2, 5 min). (B) Analysis of AuMSS and AuMSS/PEI/RBC (100 and 200 µg/mL) with or without AO encapsulation and NIR irradiation. Positive control (K^+): cells treated with ethanol; Negative control (K^-): cells without nanoparticles incubation; K NIR: cells without nanoparticles incubation and irradiated with NIR laser. Data are presented as mean ± s.d, (***p<0.001, ****p < 0.0001, n.s. non-significant), n= 5.

The cellular death mediated by single PTT is consistent with the previous *in vitro* PTT experiments, wherein AuMSS nanoformulations induced a temperature increase of ≈30ºC. However, it was observed that AuMSS/PEI/RBC nanorods induced a slightly higher cellular death in single PTT at both tested concentrations, when compared with AuMSS nanorods (*i.e.,* cell viability of 54% vs 61% at 100 µg/mL and 9% vs 17% at 200 µg/mL). This difference can be attributed to the higher internalization of AuMSS/PEI/RBC nanorods compared to AuMSS nanorods.

Finally, the therapeutic effect of AuMSS nanoformulations was further confirmed by the Live/Dead assay (Figure 9). The CLSM images show a zone with green fluorescence that corresponds to calcein-stained cells (live cells), whereas a zone with red fluorescence corresponds to dead cells stained with PI. The AuMSS, AuMSS/PEI/RBC, and AuMSS/PEI/RBC_AO treated with NIR groups exhibited a well-defined red region within the area irradiated by the NIR laser (identified with the white circles). This observation corroborates that AuMSS nanoformulations can be activated by NIR laser irradiation, inducing a localized cancer hyperthermia. Moreover, it is also possible to observe that AuMSS/PEI/RBC_AO nanorods W/ NIR (*i.e.,* the combination of NIR laser irradiation and AO delivery) presented a higher area of PI-stained HeLa cells than AuMSS/PEI/RBC nanorods. In fact, the red zone slightly exceeds the area irradiated by the NIR laser, which can be attributed to the enhanced therapeutic effect of the PTT/AO delivery combination. Additionally, the AuMSS/PEI/RBC_AO nanorods W/O NIR (*i.e.,*

without NIR laser irradiation) presented a smaller red zone than those irradiated by NIR laser. This difference corresponds to HeLa cells death solely due to the single action of AO encapsulated in the nanoparticles.

Altogether, the obtained results demonstrate that the therapeutic combination (*i.e.*, AO delivery and photothermal effect) improved the therapeutic potential of AuMSS/PEI/RBC nanomaterials, leading to more than > 90% of HeLa cells death. These results are consistent with the nanoparticles' photothermal data, suggesting that they can directly induce the death of the HeLa cells and/or sensitize the cells for the action of AO. Moreover, these data are in accordance with reports in the literature, where the combination of PTT with drug delivery has been shown to enhance the cytotoxic effect of nanoparticles (Moreira et al., 2018b; Nam et al., 2018; Oei et al., 2015; Shrestha et al., 2019). Overall, our findings suggest that the functionalization with PEI/RBC-derived membranes can improve the biological performance of AuMSS and contribute to the effectiveness of the combinatorial treatment for cervical cancer.

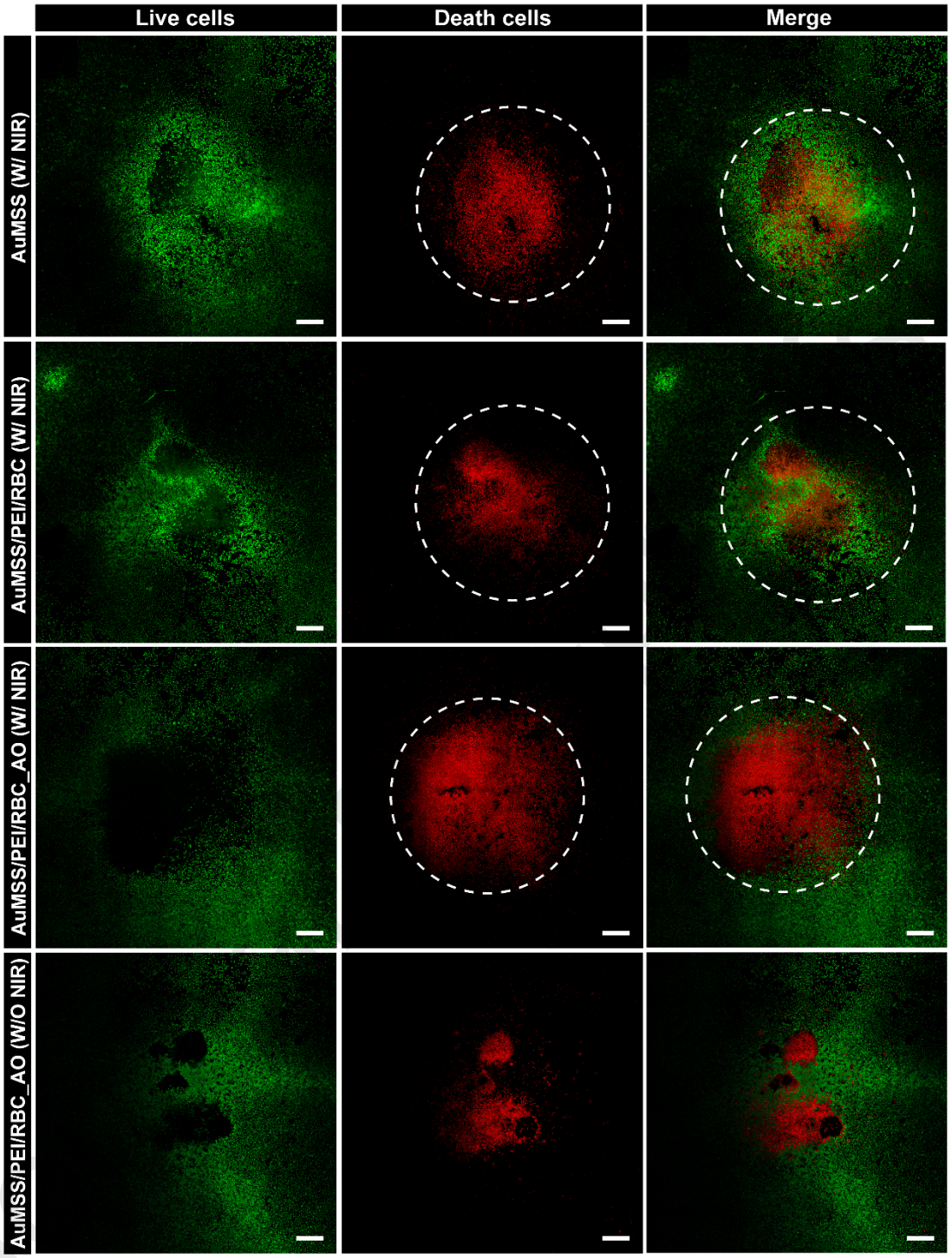

Figure 9 - CLSM analysis of the therapeutic potential of AuMSS nanomaterials in HeLa cancer cells. (A) Live/dead CLSM images depicting the cytotoxic activity of AuMSS, AuMSS/PEI/RBC, and AuMSS/PEI/RBC_AO nanorods at 200 µg/mL. White circles indicate the total area irradiated by the NIR laser (808 nm, 1.7 W/cm^2, 5 min). W/O NIR: without NIR laser irradiation; W/ NIR with NIR laser irradiation. Green channel: Calcein-AM stained cells. Red channel: PI-stained cells; Scale bar = 500 µm.

4. Conclusion

Nanomaterials-mediated PTT is emerging as a promising strategy for cancer treatment, either as a standalone or combinatorial cancer therapeutic approach. Among the different nanostructures that are able to mediate a photothermal effect, AuMSS nanorods

have been widely explored for cancer therapy applications due to their unique physicochemical properties, that allow the simultaneous combination of PTT, drug delivery, and bioimaging. Despite the huge potential of nanomedicines to deliver cargo and mediate cancer cells death, it is reported that once administrated nanoparticles can be coated with blood proteins, forming a protein corona, that affects nanomedicines' circulation time, biodistribution, and therapeutic performance. Therefore, it becomes urgent to develop novel alternatives to improve nanoparticles' pharmacokinetics, starting with the blood circulation time. With that in mind, herein, RBC-derived membranes and PEI were combined for the first time to modify the AuMSS nanorods.

The results revealed that PEI/RBC-derived membranes' functionalization improves nanoparticles' stability, and biocompatibility, namely by decreasing the blood hemolysis to safe levels. Such results can be attributed to the neutralization of nanoparticles' surface charge, transitioning from -26 to -16 mV. Additionally, the modification with RBC-derived membranes also improved the nanoparticles' cellular internalization. The PEI/RBC-derived membranes' functionalization induced a more sustained AO release, which could be accelerated upon irradiation with an NIR laser. Moreover, the *in vitro* antitumoral studies revealed that the combinatorial treatment (*i.e.,* PTT and AO delivery) mediated by AuMSS/PEI/RBC_AO nanorods improved the nanoparticles' therapeutic effect when compared with PTT and chemotherapy alone. Overall, the attained data confirm the successful AuMSS modification with PEI/RBC-derived membranes, which enhances the biocompatibility, and the potential for being applied as PTT and chemotherapeutic nanomedicines for the combinatorial treatment of cancer. Additionally, these results reinforce the multifunctional potential of AuMSS nanomedicines and encourage researchers to continue to explore novel surface modifications and PTT/chemo combinations to improve nanoparticles' pharmacokinetic profile and therapeutic performance. Particularly, the combination of biomimetic coatings (*e.g.,* RBC and cancer cells-derived membranes) with targeting moieties, materials responsive to different stimuli (*e.g.,* pH, ROS), as well as, the simultaneous conjugation of chemo-PTT with other therapeutic modalities (*e.g.,* immunotherapy), will improve AuMSS nanorods' retention in the tumor tissue and create a safer and more effective cancer treatment, which consequently will accelerate their translation to the clinical practice.

Acknowledgments

This work was developed within the scope of the CICS-UBI projects UIDB/00709/2020 and UIDP/00709/2020, financed by national funds through the Portuguese Foundation for Science and Technology/MCTES. The funding from PTDC/BTA-BTA/0696/2020 and 2022.06320.PTDC is also acknowledged. Carolina F. Rodrigues acknowledges for her Ph.D. fellowship from FCT (SFRH/BD/144680/2019). The funders had no role in the decision to publish or in the preparation of the manuscript.

Authorship contribution statement

Carolina F. Rodrigues: Investigation, Conceptualization, Formal analysis, Writing–original draft. Ilídio J. Correia: Funding acquisition, Supervision, Writing – review & editing. André F. Moreira: Conceptualization, Supervision, Writing–review & editing.

Conflict of interest

The authors declare no financial or commercial conflict of interest.

5. References

Abadeer, N.S., Brennan, M.R., Wilson, W.L., Murphy, C.J., 2014. Distance and plasmon wavelength dependent fluorescence of molecules bound to silica-coated gold nanorods. ACS nano 8, 8392-8406.

Al-Lazikani, B., Banerji, U., Workman, P., 2012. Combinatorial drug therapy for cancer in the post-genomic era. Nature biotechnology 30, 679-692.

Alves, C.G., Lima-Sousa, R., Melo, B.L., Moreira, A.F., Correia, I.J., de Melo-Diogo, D., 2022. Heptamethine cyanine-loaded nanomaterials for cancer immuno-photothermal/photodynamic therapy: a review. Pharmaceutics 14, 1015.

Bebesi, T., Kitka, D., Gaál, A., Szigyártó, I.C., Deák, R., Beke-Somfai, T., Koprivanacz, K., Juhász, T., Bóta, A., Varga, Z., 2022. Storage conditions determine the characteristics of red blood cell derived extracellular vesicles. Scientific reports 12, 977.

Blat, A., Dybas, J., Kaczmarska, M., Chrabaszcz, K., Bulat, K., Kostogrys, R.B., Cernescu, A., Malek, K., Marzec, K.M., 2019. An analysis of isolated and intact rbc membranes—A comparison of a semiquantitative approach by means of FTIR, Nano-FTIR, and Raman Spectroscopies. Analytical chemistry 91, 9867-9874.

Corbo, C., Molinaro, R., Parodi, A., Toledano Furman, N.E., Salvatore, F., Tasciotti, E., 2016. The impact of nanoparticle protein corona on cytotoxicity, immunotoxicity and target drug delivery. Nanomedicine 11, 81-100.

de Melo-Diogo, D., Lima-Sousa, R., Alves, C.G., Correia, I.J., 2019. Graphene family nanomaterials for application in cancer combination photothermal therapy. Biomaterials science 7, 3534-3551.

de Melo-Diogo, D., Pais-Silva, C., Dias, D.R., Moreira, A.F., Correia, I.J., 2017. Strategies to improve cancer photothermal therapy mediated by nanomaterials. Advanced healthcare materials 6, 1700073.

Dias, D.R., Moreira, A.F., Correia, I.J., 2016. The effect of the shape of gold core–mesoporous silica shell nanoparticles on the cellular behavior and tumor spheroid penetration. Journal of Materials Chemistry B 4, 7630-7640.

Fernandes, N., Rodrigues, C.F., Moreira, A.F., Correia, I.J., 2020. Overview of the application of inorganic nanomaterials in cancer photothermal therapy. Biomaterials science 8, 2990-3020.

Gao, W., Hu, C.-M.J., Fang, R.H., Luk, B.T., Su, J., Zhang, L., 2013. Surface functionalization of gold nanoparticles with red blood cell membranes. Advanced materials (Deerfield Beach, Fla.) 25, 3549.

Gavas, S., Quazi, S., Karpiński, T.M., 2021. Nanoparticles for cancer therapy: current progress and challenges. Nanoscale research letters 16, 173.

Gonçalves, A.S., Rodrigues, C.F., Fernandes, N., de Melo-Diogo, D., Ferreira, P., Moreira, A.F., Correia, I.J., 2022. IR780 loaded gelatin-PEG coated gold core silica shell nanorods for cancer-targeted photothermal/photodynamic therapy. Biotechnology and Bioengineering 119, 644-656.

879 Gonçalves, A.S., Rodrigues, C.F., Moreira, A.F., Correia, I.J., 2020. Strategies to
880 improve the photothermal capacity of gold-based nanomedicines. Acta Biomaterialia
881 116, 105-137.

882 Gong, B., Shen, Y., Li, H., Li, X., Huan, X., Zhou, J., Chen, Y., Wu, J., Li, W., 2021.
883 Thermo-responsive polymer encapsulated gold nanorods for single continuous wave
884 laser-induced photodynamic/photothermal tumour therapy. Journal of
885 nanobiotechnology 19, 1-14.

886 Gorelikov, I., Matsuura, N., 2008. Single-step coating of mesoporous silica on
887 cetyltrimethyl ammonium bromide-capped nanoparticles. Nano letters 8, 369-373.

888 Guimaraes, R.S., Rodrigues, C.F., Fernandes, N., de Melo-Diogo, D., Ferreira, P.,
889 Correia, I.J., Moreira, A.F., 2021. Combinatorial delivery of doxorubicin and acridine
890 orange by gold core silica shell nanospheres functionalized with poly (ethylene glycol)
891 and 4-methoxybenzamide for cancer targeted therapy. Journal of Inorganic Biochemistry
892 219, 111433.

893 Hu, X., Gao, X., 2011. Multilayer coating of gold nanorods for combined stability and
894 biocompatibility. Physical Chemistry Chemical Physics 13, 10028-10035.

895 Jacinto, T.A., Rodrigues, C.F., Moreira, A.F., Miguel, S.P., Costa, E.C., Ferreira, P.,
896 Correia, I.J., 2020. Hyaluronic acid and vitamin E polyethylene glycol succinate
897 functionalized gold-core silica shell nanorods for cancer targeted photothermal therapy.
898 Colloids and Surfaces B: Biointerfaces 188, 110778.

899 Jin, J., Bhujwalla, Z.M., 2020. Biomimetic nanoparticles camouflaged in cancer cell
900 membranes and their applications in cancer theranostics. Frontiers in Oncology, 1560.

901 Kang, J.K., Kim, J.C., Shin, Y., Han, S.M., Won, W.R., Her, J., Park, J.Y., Oh, K.T., 2020.
902 Principles and applications of nanomaterial-based hyperthermia in cancer therapy.
903 Archives of pharmacal research 43, 46-57.

904 Kennedy, L.C., Bickford, L.R., Lewinski, N.A., Coughlin, A.J., Hu, Y., Day, E.S., West,
905 J.L., Drezek, R.A., 2011. A new era for cancer treatment: gold-nanoparticle-mediated
906 thermal therapies. Small 7, 169-183.

907 Khafaji, M., Zamani, M., Golizadeh, M., Bavi, O., 2019. Inorganic nanomaterials for
908 chemo/photothermal therapy: a promising horizon on effective cancer treatment.
909 Biophysical reviews 11, 335-352.

910 Li, Z., Chen, Y., Yang, Y., Yu, Y., Zhang, Y., Zhu, D., Yu, X., Ouyang, X., Xie, Z., Zhao,
911 Y., 2019. Recent advances in nanomaterials-based chemo-photothermal combination
912 therapy for improving cancer treatment. Frontiers in bioengineering and biotechnology
913 7, 293.

914 Liu, B., Wang, W., Fan, J., Long, Y., Xiao, F., Daniyal, M., Tong, C., Xie, Q., Jian, Y., Li,
915 B., 2019. RBC membrane camouflaged prussian blue nanoparticles for gamabutolin
916 loading and combined chemo/photothermal therapy of breast cancer. Biomaterials 217,
917 119301.

918 Liu, W., Ruan, M., Wang, Y., Song, R., Ji, X., Xu, J., Dai, J., Xue, W., 2018.
919 Light-triggered biomimetic nanoerythrocyte for tumor-targeted lung metastatic
920 combination therapy of malignant melanoma. Small 14, 1801754.

921 Liu, Z., Xie, H., Wang, T., 2023. Erythrocyte–Cancer Hybrid Membrane-Camouflaged
922 Prussian Blue Nanoparticles with Enhanced Photothermal Therapy in Tumors. ACS
923 Omega.

924 Luo, D., Wang, X., Burda, C., Basilion, J.P., 2021. Recent development of gold
925 nanoparticles as contrast agents for cancer diagnosis. Cancers 13, 1825.

926 Mahmoudi, M., Bertrand, N., Zope, H., Farokhzad, O.C., 2016. Emerging understanding
927 of the protein corona at the nano-bio interfaces. Nano Today 11, 817-832.

928 Mazur, M., Włoch, A., Bahri, F., Pruchnik, H., Pawlak, A., Obmińska-Mrukowicz, B.,
929 Maciejewska, G., Gładkowski, W., 2020. Chemoenzymatic synthesis of enantiomeric,
930 bicyclic δ-halo-γ-lactones with a cyclohexane ring, their biological activity and interaction
931 with biological membranes. Biomolecules 10, 95.

932 Mima, Y., Hashimoto, Y., Shimizu, T., Kiwada, H., Ishida, T., 2015. Anti-PEG IgM is a
933 major contributor to the accelerated blood clearance of polyethylene glycol-conjugated
934 protein. Molecular pharmaceutics 12, 2429-2435.

935 Moreira, A.F., Gaspar, V.M., Costa, E.C., de Melo-Diogo, D., Machado, P., Paquete,
936 C.M., Correia, I.J., 2014. Preparation of end-capped pH-sensitive mesoporous silica
937 nanocarriers for on-demand drug delivery. European Journal of Pharmaceutics and
938 Biopharmaceutics 88, 1012-1025.

939 Moreira, A.F., Rodrigues, C.F., Reis, C.A., Costa, E.C., Correia, I.J., 2018a. Gold-core
940 silica shell nanoparticles application in imaging and therapy: A review. Microporous and
941 Mesoporous Materials 270, 168-179.

942 Moreira, A.F., Rodrigues, C.F., Reis, C.A., Costa, E.C., Ferreira, P., Correia, I.J., 2018b.
943 Development of poly-2-ethyl-2-oxazoline coated gold-core silica shell nanorods for
944 cancer chemo-photothermal therapy. Nanomedicine 13, 2611-2627.

945 Moreira, A.F., Rodrigues, C.F., Jacinto, T.A., Miguel, S.P., Costa, E.C., Correia, I.J.,
946 2020. Poly (vinyl alcohol)/chitosan layer-by-layer microneedles for cancer chemo-
947 photothermal therapy. International Journal of Pharmaceutics 576, 118907.

948 Nam, J., Son, S., Ochyl, L.J., Kuai, R., Schwendeman, A., Moon, J.J., 2018. Chemo-
949 photothermal therapy combination elicits anti-tumor immunity against advanced
950 metastatic cancer. Nature communications 9, 1074.

951 Oei, A.L., Vriend, L.E., Crezee, J., Franken, N.A., Krawczyk, P.M., 2015. Effects of
952 hyperthermia on DNA repair pathways: one treatment to inhibit them all. Radiation
953 Oncology 10, 1-13.

954 Perry, J.L., Reuter, K.G., Kai, M.P., Herlihy, K.P., Jones, S.W., Luft, J.C., Napier, M.,
955 Bear, J.E., DeSimone, J.M., 2012. PEGylated PRINT nanoparticles: the impact of PEG
956 density on protein binding, macrophage association, biodistribution, and
957 pharmacokinetics. Nano letters 12, 5304-5310.

958 Qi, Z., Shi, J., Zhang, Z., Cao, Y., Li, J., Cao, S., 2019. PEGylated graphene oxide-
959 capped gold nanorods/silica nanoparticles as multifunctional drug delivery platform with
960 enhanced near-infrared responsiveness. Materials Science and Engineering: C 104,
961 109889.

962 Rao, L., Bu, L.L., Xu, J.H., Cai, B., Yu, G.T., Yu, X., He, Z., Huang, Q., Li, A., Guo, S.S.,
963 2015. Red blood cell membrane as a biomimetic nanocoating for prolonged circulation
964 time and reduced accelerated blood clearance. Small 11, 6225-6236.

965 Reis, C.A., Rodrigues, C.F., Moreira, A.F., Jacinto, T.A., Ferreira, P., Correia, I.J., 2019.
966 Development of gold-core silica shell nanospheres coated with poly-2-ethyl-oxazoline
967 and β-cyclodextrin aimed for cancer therapy. Materials Science and Engineering: C 98,
968 960-968.

969 Ren, H., Liu, J., Li, Y., Wang, H., Ge, S., Yuan, A., Hu, Y., Wu, J., 2017. Oxygen self-
970 enriched nanoparticles functionalized with erythrocyte membranes for long circulation
971 and enhanced phototherapy. Acta biomaterialia 59, 269-282.

972 Rodrigues, C.F., Alves, C.G., Lima-Sousa, R., Moreira, A.F., de Melo-Diogo, D., Correia,
973 I.J., 2020. Inorganic-based drug delivery systems for cancer therapy, Advances and
974 Avenues in the Development of Novel Carriers for Bioactives and Biological Agents.
975 Elsevier, pp. 283-316.

976 Rodrigues, C.F., Fernandes, N., de Melo-Diogo, D., Ferreira, P., Correia, I.J., Moreira,
977 A.F., 2021. HA/PEI-coated acridine orange-loaded gold-core silica shell nanorods for
978 cancer-targeted photothermal and chemotherapy. Nanomedicine 16, 2569-2586.

979 Rodrigues, C.F., Fernandes, N., de Melo-Diogo, D., Correia, I.J., Moreira, A.F., 2022.
980 Cell-Derived Vesicles for Nanoparticles' Coating: Biomimetic Approaches for Enhanced
981 Blood Circulation and Cancer Therapy. Advanced Healthcare Materials 11, 2201214.

982 Rodrigues, C.F., Jacinto, T.A., Moreira, A.F., Costa, E.C., Miguel, S.P., Correia, I.J.,
983 2019a. Functionalization of AuMSS nanorods towards more effective cancer therapies.
984 Nano Research 12, 719-732.

985 Rodrigues, C.F., Reis, C.A., Moreira, A.F., Ferreira, P., Correia, I.J., 2019b. Optimization
986 of gold core-mesoporous silica shell functionalization with TPGS and PEI for cancer
987 therapy. Microporous and Mesoporous Materials 285, 1-12.

988 Sedlacek, O., Hoogenboom, R., 2020. Drug Delivery Systems Based on Poly
989 (2-oxazoline) s and Poly (2-oxazine) s. Advanced Therapeutics 3, 1900168.

990 Seo, S.-H., Joe, A., Han, H.-W., Manivasagan, P., Jang, E.-S., 2022. Methylene Blue-
991 Loaded Mesoporous Silica-Coated Gold Nanorods on Graphene Oxide for Synergistic
992 Photothermal and Photodynamic Therapy. Pharmaceutics 14, 2242.

993 Shajari, D., Bahari, A., Gill, P., Mohseni, M., 2017. Synthesis and tuning of gold nanorods
994 with surface plasmon resonance. Optical Materials 64, 376-383.

995 Shrestha, B., Tang, L., Romero, G., 2019. Nanoparticles-mediated combination
996 therapies for cancer treatment. Advanced Therapeutics 2, 1900076.

997 Su, G., Yang, C., Zhu, J.-J., 2015. Fabrication of gold nanorods with tunable longitudinal
998 surface plasmon resonance peaks by reductive dopamine. Langmuir 31, 817-823.

999 Suk, J.S., Xu, Q., Kim, N., Hanes, J., Ensign, L.M., 2016. PEGylation as a strategy for
1000 improving nanoparticle-based drug and gene delivery. Advanced drug delivery reviews
1001 99, 28-51.

Taylor, M.L., Wilson Jr, R.E., Amrhein, K.D., Huang, X., 2022. Gold nanorod-assisted photothermal therapy and improvement strategies. Bioengineering 9, 200.

Vermeulen, L.M., De Smedt, S.C., Remaut, K., Braeckmans, K., 2018. The proton sponge hypothesis: Fable or fact? European Journal of Pharmaceutics and Biopharmaceutics 129, 184-190.

Wang, F., Ye, X., Wu, Y., Wang, H., Sheng, C., Peng, D., Chen, W., 2019. Time interval of two injections and first-dose dependent of accelerated blood clearance phenomenon induced by PEGylated liposomal gambogenic acid: the contribution of PEG-specific IgM. Journal of Pharmaceutical Sciences 108, 641-651.

Wang, S., Xi, W., Cai, F., Zhao, X., Xu, Z., Qian, J., He, S., 2015. Three-photon luminescence of gold nanorods and its applications for high contrast tissue and deep in vivo brain imaging. Theranostics 5, 251.

Wang, X., Li, H., Liu, X., Tian, Y., Guo, H., Jiang, T., Luo, Z., Jin, K., Kuai, X., Liu, Y., 2017. Enhanced photothermal therapy of biomimetic polypyrrole nanoparticles through improving blood flow perfusion. Biomaterials 143, 130-141.

Wilhelm, S., Tavares, A.J., Dai, Q., Ohta, S., Audet, J., Dvorak, H.F., Chan, W.C., 2016. Analysis of nanoparticle delivery to tumours. Nature reviews materials 1, 1-12.

Xia, Q., Zhang, Y., Li, Z., Hou, X., Feng, N., 2019. Red blood cell membrane-camouflaged nanoparticles: a novel drug delivery system for antitumor application. Acta Pharmaceutica Sinica B 9, 675-689.

Ye, S., Wang, F., Fan, Z., Zhu, Q., Tian, H., Zhang, Y., Jiang, B., Hou, Z., Li, Y., Su, G., 2019. Light/pH-triggered biomimetic red blood cell membranes camouflaged small molecular drug assemblies for imaging-guided combinational chemo-photothermal therapy. ACS applied materials & interfaces 11, 15262-15275.

Zakeri, A., Kouhbanani, M.A.J., Beheshtkhoo, N., Beigi, V., Mousavi, S.M., Hashemi, S.A.R., Karimi Zade, A., Amani, A.M., Savardashtaki, A., Mirzaei, E., 2018. Polyethylenimine-based nanocarriers in co-delivery of drug and gene: A developing horizon. Nano reviews & experiments 9, 1488497.

Zhang, Y., Li, M., Gao, X., Chen, Y., Liu, T., 2019. Nanotechnology in cancer diagnosis: progress, challenges and opportunities. Journal of hematology & oncology 12, 1-13.

Zhou, Y., Quan, G., Wu, Q., Zhang, X., Niu, B., Wu, B., Huang, Y., Pan, X., Wu, C., 2018. Mesoporous silica nanoparticles for drug and gene delivery. Acta pharmaceutica sinica B 8, 165-177.

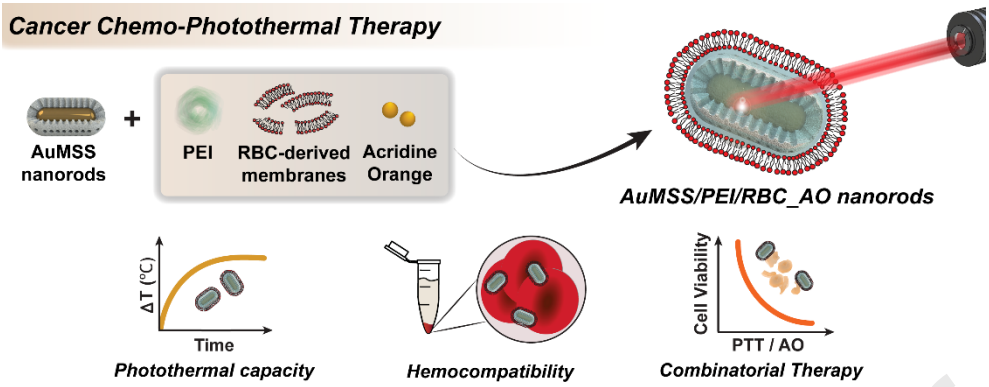

Declaration of interests

☒ The authors declare that they have no known competing financial interests or personal relationships that could have appeared to influence the work reported in this paper.

☐ The authors declare the following financial interests/personal relationships which may be considered as potential competing interests: